



Originally published as:

Hannemann, K., Krüger, F., Dahm, T., Lange, D. (2017): Structure of the oceanic lithosphere and upper mantle north of the Gloria Fault in the eastern mid-Atlantic by receiver function analysis. - *Journal of Geophysical Research*, 122, 10, pp. 7927—7950.

DOI: <http://doi.org/10.1002/2016JB013582>

## RESEARCH ARTICLE

10.1002/2016JB013582

## Key Points:

- First evidence of a normal mantle transition zone in the mid-Atlantic from RFs in the deep ocean
- Improve signal quality of OBS receiver functions (RFs) by quantitative evaluation and beamforming
- Body wave imaging of discontinuities in mid-oceanic lithosphere and upper mantle using OBS data

## Correspondence to:

K. Hannemann,  
khannemann@geomar.de

## Citation:

Hannemann, K., F. Krüger, T. Dahm, and D. Lange (2017), Structure of the oceanic lithosphere and upper mantle north of the Gloria Fault in the eastern mid-Atlantic by receiver function analysis, *J. Geophys. Res. Solid Earth*, 122, 7927–7950, doi:10.1002/2016JB013582.



Received 22 SEP 2016

Accepted 11 AUG 2017

Accepted article online 15 AUG 2017

Published online 13 OCT 2017

## Structure of the oceanic lithosphere and upper mantle north of the Gloria Fault in the eastern mid-Atlantic by receiver function analysis

Katrin Hannemann<sup>1</sup> , Frank Krüger<sup>2</sup>, Torsten Dahm<sup>2,3</sup>, and Dietrich Lange<sup>1</sup> 

<sup>1</sup>GEOMAR-Helmholtz Centre for Ocean Research Kiel, Kiel, Germany, <sup>2</sup>Institute of Earth and Environmental Science, University of Potsdam, Potsdam, Germany, <sup>3</sup>Section 2.1, Physics of Earthquakes and Volcanoes, GFZ Potsdam, Potsdam, Germany

**Abstract** Receiver functions (RF) have been used for several decades to study structures beneath seismic stations. Although most available stations are deployed on shore, the number of ocean bottom station (OBS) experiments has increased in recent years. Almost all OBSs have to deal with higher noise levels and a limited deployment time (~1 year), resulting in a small number of usable records of teleseismic earthquakes. Here we use OBSs deployed as midaperture array in the deep ocean (4.5–5.5 km water depth) of the eastern mid-Atlantic. We use evaluation criteria for OBS data and beamforming to enhance the quality of the RFs. Although some stations show reverberations caused by sedimentary cover, we are able to identify the Moho signal, indicating a normal thickness (5–8 km) of oceanic crust. Observations at single stations with thin sediments (300–400 m) indicate that a probable sharp lithosphere-asthenosphere boundary (LAB) might exist at a depth of ~70–80 km which is in line with LAB depth estimates for similar lithospheric ages in the Pacific. The mantle discontinuities at ~410 km and ~660 km are clearly identifiable. Their delay times are in agreement with PREM. Overall the usage of beam-formed earthquake recordings for OBS RF analysis is an excellent way to increase the signal quality and the number of usable events.

### 1. Introduction

More than 70% of the Earth is covered by oceans, and the majority of the oceanic crust is not affected by recent volcanic or tectonic activities like mid-ocean ridges, subduction zones, or hot spots. The *P* wave velocity-depth structure of the oceanic crust and uppermost mantle has been characterized by active geophysical experiments [e.g., White *et al.*, 1992]. Deeper structures in the oceanic lithosphere and upper mantle are studied using broadband ocean bottom stations (OBSs) [e.g., Suetsugu and Shiobara, 2014]. In recent years, several passive large-scale experiments with OBSs have been conducted [e.g., Friederich and Meier, 2008; Barruol and Sigloch, 2013; Gao and Schwartz, 2015; Lin *et al.*, 2016; Ryberg *et al.*, 2017]. Nevertheless, most of the OBS studies are located at mid-ocean ridges [e.g., Shen *et al.*, 1998a; Tilmann and Dahm, 2008; Jokat *et al.*, 2012; Grevemeyer *et al.*, 2013; Hermann and Jokat, 2013; Schlindwein *et al.*, 2013, 2015], hot spots [e.g., Suetsugu *et al.*, 2007; Barruol and Sigloch, 2013; Davy *et al.*, 2014; Geissler *et al.*, 2016; Ryberg *et al.*, 2017], subduction zones [e.g., Suetsugu *et al.*, 2010; Kopp *et al.*, 2011; Laigle *et al.*, 2013; Ruiz *et al.*, 2013; Grevemeyer *et al.*, 2015; Janiszewski and Abers, 2015] or the transition from continental crust to oceanic crust [e.g., Czuba *et al.*, 2011; Grad *et al.*, 2012; Libak *et al.*, 2012; Suckro *et al.*, 2012; Monna *et al.*, 2013; Altenbernd *et al.*, 2014; Kalberg and Gohl, 2014], and are thus not representative of undisturbed oceanic crust and mantle.

Most of our knowledge of the oceanic mantle is based on global surface wave tomography [e.g., Romanowicz, 2009], with rather good path coverage in the oceans but low resolution for sharp discontinuities. Furthermore, studies using land based stations at teleseismic distances have been conducted to analyze underside reflections to resolve oceanic mantle structures (PP and SS precursors) [Gossler and Kind, 1996; Gu *et al.*, 1998; Flanagan and Shearer, 1998; Gu and Dziewonski, 2002; Deuss *et al.*, 2013; Saki *et al.*, 2015]. Both methods lack spatial resolution. On the other hand, receiver function (RF) analysis provides a strong tool to image discontinuities in the lithosphere and the upper mantle down to the transition zone with high lateral resolution [e.g., Vinnik, 1977; Langston, 1979]. So far only a limited number of receiver function (RF) studies of undisturbed oceanic lithosphere have been conducted using 500 m deep borehole stations and OBSs [Suetsugu *et al.*, 2005; Kawakatsu *et al.*, 2009; Olugboji *et al.*, 2016].

This study focuses on OBS RFs in the eastern mid-Atlantic in the vicinity of the Eurasian-African plate boundary, in which—to our knowledge—no OBS RF study has previously been done. We target major discontinuities within the oceanic lithosphere and mantle. The Mohorovičić discontinuity (Moho) marks the boundary between oceanic crust and mantle and is expected in depths between 5 and 8 km [e.g., *White et al.*, 1992]. Thickened or thinned oceanic crust may be related to overthrusting, underplating, or basin formation. The RF phase of the Moho arrives only 1 or 2 s after the dominant *P* phase [e.g., *Kawakatsu et al.*, 2009] and therefore requires high-frequency data [*Audet*, 2016], and a good signal-to-noise ratio (SNR). Furthermore, it is often masked by sediment reverberations which hamper a direct interpretation of the Moho signal [*Audet*, 2016; *Kawakatsu and Abe*, 2016].

The lithosphere-asthenosphere boundary (LAB) beneath the oceans is often imaged using surface waves [e.g., *Romanowicz*, 2009; *Takeo et al.*, 2013, 2016; *Lin et al.*, 2016], SS waveforms [e.g., *Rychert et al.*, 2012], RFs employing land stations [e.g., *Li et al.*, 2000; *Kumar and Kawakatsu*, 2011], or OBSs [e.g., *Kawakatsu et al.*, 2009; *Olugboji et al.*, 2016]. Most of the discussed models of the LAB [*Kawakatsu et al.*, 2009; *Fischer et al.*, 2010; *Olugboji et al.*, 2013] include thermal control, changes in rheology, dehydration, anisotropy, or partial melt. Experiments with polycrystalline materials [*Takei et al.*, 2014; *Yamauchi and Takei*, 2016] at subsolidus temperatures indicate that solid state mechanism such as diffusionally accommodated grain boundary sliding play an important role for *S* wave velocity decrease with rising temperature in the oceanic lithosphere [*Yamauchi and Takei*, 2016, Figure 20]. Besides the depth of the LAB, the sharpness of the discontinuity is of interest. A relatively smooth transition would be expected if the position of the LAB is purely thermally controlled [*Olugboji et al.*, 2013] and a sharp boundary if it is controlled by composition (e.g., abrupt change in water content [*Karato and Jung*, 1998]). Both of these cases mark end-member models, and a variety of intermediate models may be possible (e.g., a gradual change in the water content leading to a smooth transition). For example, a land-based *S* wave RF study of oceanic lithosphere in subduction zones [*Kumar and Kawakatsu*, 2011] supports the model of thermal control, but the observed scatter in the observations indicates additional controlling factors. Observations of the oceanic LAB indicate a diffuse age-dependent boundary in young oceans and a sharp age-independent LAB at ~70 km in old oceans [e.g., *Fischer et al.*, 2010; *Karato*, 2012; *Olugboji et al.*, 2013]. A subsolidus model which assumes grain boundary sliding [*Karato*, 2012; *Olugboji et al.*, 2013] predicts a transition from an age-dependent diffuse LAB roughly following the 1300 K isotherm in young oceans, to a sharp discontinuity at constant depth in old oceans. The age at which this transition happens, depends on the thermal model used for the modeling and lies between 40–80 Ma [*Karato*, 2012] or between 55–75 Ma [*Olugboji et al.*, 2013].

The Lehmann discontinuity is assumed to mark the lower boundary of the asthenosphere [e.g., *Lehmann*, 1961; *Dziewonski and Anderson*, 1981; *Deuss et al.*, 2013]. It is located at around 220 km depth, and its cause is still debated [*Karato*, 1992; *Deuss and Woodhouse*, 2004]. Only a few RF [*Shen et al.*, 1998a] and SS precursor observations [*Deuss and Woodhouse*, 2002] exist of the oceanic Lehmann discontinuity.

The three global mantle discontinuities at approximately 410 km, 520 km, and 660 km depth (referred to as “410,” “520,” and “660,” respectively) are associated with phase transitions in olivine or the aluminum phases (e.g., garnet) of the mantle [e.g., *Agee*, 1998; *Helfrich*, 2000; *Deuss et al.*, 2013]. In the ocean, the mantle transition zone (MTZ), defined by the 410 and the 660, has mostly been studied by using PP and SS precursors [*Gossler and Kind*, 1996; *Gu et al.*, 1998; *Flanagan and Shearer*, 1998; *Gu and Dziewonski*, 2002; *Deuss et al.*, 2013; *Saki et al.*, 2015]. There are also some global RF studies of the MTZ [*Chevrot et al.*, 1999; *Lawrence and Shearer*, 2006; *Tauzin et al.*, 2008] and local studies focusing on the MTZ using OBS data [*Shen et al.*, 1998a; *Gilbert et al.*, 2001; *Suetsugu et al.*, 2005, 2007, 2010]. Some global studies of SS precursors suggest a thinner MTZ beneath the oceans than below the continents [*Gossler and Kind*, 1996; *Gu et al.*, 1998; *Gu and Dziewonski*, 2002]; however, *Flanagan and Shearer* [1998] (SS precursors) and *Chevrot et al.* [1999] (RF) could not observe such a correlation. The lack of correlation is also confirmed by local studies [*Shen et al.*, 1998a, 1998b; *Silveira et al.*, 2010].

Here we use data from 11 OBSs located in the eastern mid-Atlantic approximately 100 km North of the Gloria Fault (Figure 1b) to investigate the structure of the oceanic crust and upper mantle using array techniques (e.g., “delay and sum” beamforming [*Rost and Thomas*, 2002]) and receiver functions. OBS data are usually characterized by a small amount of good-quality events within a short recording period of the deployed instruments (~1 year) [*Webb*, 1998]. One of the main reasons is the often low signal-to-noise ratio (SNR) at ocean bottom stations [*Webb*, 1998; *Dahm et al.*, 2006], especially in the horizontal components. There have

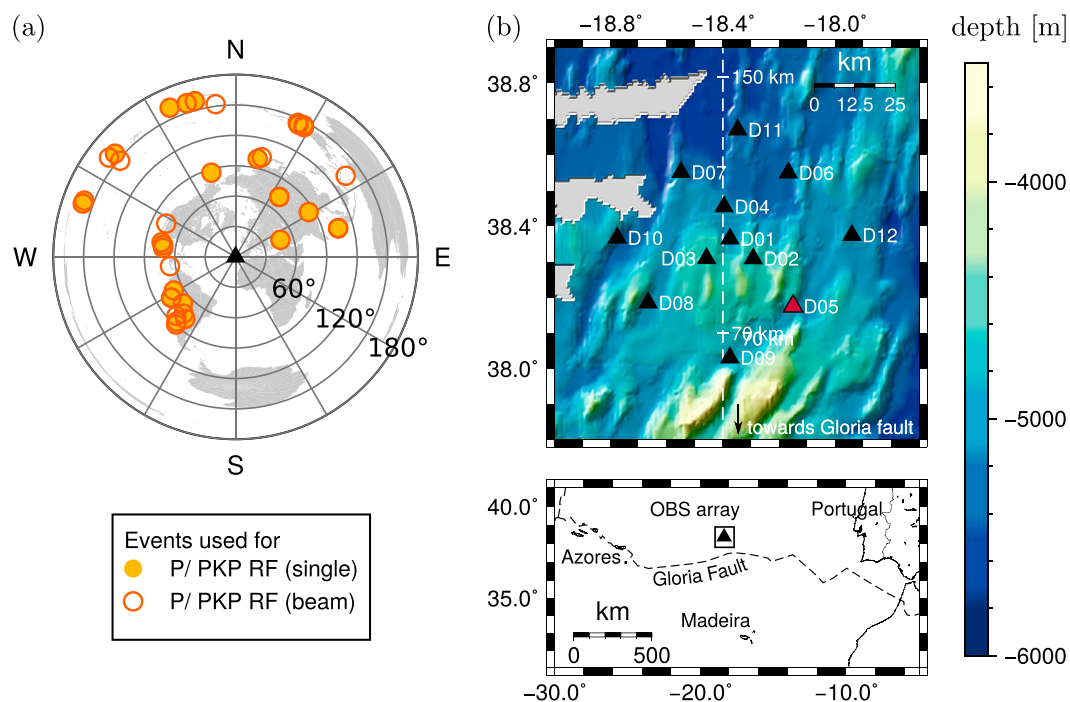


**Figure 1.** (a) Azimuthal equidistant plot of events used for RF analysis indicated as filled yellow circles (P and PKP single-station RFs) and as open orange circles (P and PKP beam RFs). The event details are listed in Table C1 (in the Appendix). (b) The top map shows the array configuration for the OBS. The color scale shows the water depth (EMEP, Task Group for the Extension of the Continental Shelf). The white dashed lines indicate the distance to the Gloria Fault. The red triangle marks station D05 which has two clamped seismometer components. The black and white map shows the location of the OBS array within the eastern mid-Atlantic and the dashed line indicates the Eurasian-African plate boundary (Gloria Fault) [Bird, 2003].

been different strategies to increase the number of usable events: either by reinstalling the OBS at the same site (e.g., Cascadia Initiative) [Janiszewski and Abers, 2015] or recently by using array techniques [Thomas and Laske, 2015]. The latter is known to increase the SNR of an event by coherent stacking of the observed signals [Rost and Thomas, 2002]. It uses the event’s azimuth and the slowness of the considered phase for the estimation of time delays between the stations which are then removed before stacking the single station recordings (beamforming) (for further details, see Rost and Thomas [2002]). The experiment presented here is designed in such a way that the stations form a midaperture array with interstation distances of 10–20 km and a maximum aperture of 75 km (Figure 1b). This design allows us to stack all stations to enhance phases originating from the deeper parts of the upper mantle. Additionally, we employ a quality control by using evaluation criteria such as relative spike position within the deconvolution time window and search for an optimal deconvolution length to improve the SNR of each RF. Furthermore, we analyze the RFs from single OBSs, stacks of all stations and beams in different frequency bands and compare amplitudes and delay times of the RFs with synthetic data.

## 2. Data

We use recordings of 11 OBSs that were installed in the deep sea (4.5–5.5 km water depth) of the eastern mid-Atlantic in 2011 (Figure 1b). These stations are equipped with three-component broadband seismometers (Guralp CMG-40T, 60 s—50 Hz) and hydrophones (HighTechInc HTI-04-PCA/ULF, 100 s—8 kHz, flat instrument response down to 5 s, at D08 down to 2 s) and recorded 100 Hz data. To obtain an accurate clock drift, we use ambient noise cross correlation and compare it to the drift calculated from the synchronization with GPS to reveal static time offsets [Hannemann et al., 2014]. Subsequently, we use the pyrocko toolbox (emolch.github.io/pyrocko) to apply a time correction by inserting and deleting samples. A twelfth station (D05) has not been used for the analysis because of two clamped seismometer components.

For the free fall OBSs used in this study, the orientation of the vertical component is aligned by a gimbaling system [Stähler et al., 2016]. Since for the OBS data the orientation of the horizontal components is unknown,

we test  $P$  phase polarization and Rayleigh and Love waves [Thorwart, 2006; Stachnik et al., 2012; Sumy et al., 2015] to align the horizontal components to the north and east (see Appendix A for details).

We use, in the following, the results of the  $P$  phase for the rotation of the horizontal traces, because we find from a frequency-wave number analysis with a moving time window using the vertical traces [Rost and Thomas, 2002] that the estimated back azimuths of the  $P$  phases are more precise than those of the Rayleigh phases. They show on average a smaller deviation from the expected back azimuths [see also Thorwart, 2006].

For the RF calculation, we examine all events that have a body wave detection in our frequency-wave number detector with values of  $P$  between  $\sim 30^\circ$  and  $90^\circ$  epicentral distance,  $P_{\text{diff}}$  between  $\sim 90^\circ$  and  $110^\circ$  epicentral distance and  $PKP_{\text{df}}$  between  $\sim 140^\circ$  and  $160^\circ$  epicentral distance. The events finally used (single: 25, beams: 37, see Tables C1 and C2 in the Appendix) are chosen based on the evaluation criteria described below.

### 3. Methods

When the up-going compressional wave ( $P$  wave) is incident on an interface within the Earth, its upward propagating energy is partitioned into a  $P$  wave and a vertical polarized shear wave ( $SV$  wave). The latter is also referred to as  $P$ -to- $S$  ( $Ps$ ) wave conversion and is a secondary phase which arrives later than the direct  $P$  phase (i.e., the refracted  $P$  waves). The amplitudes of the  $Ps$  conversions are typically several tens of times smaller than those of the direct  $P$  phase, depending on the  $S$  wave velocity change at the discontinuity and the incidence angle [e.g., Chevrot et al., 1999; Julià, 2007]. The relative  $Ps$  amplitudes can be calculated from the ratio of the refraction coefficient  $\hat{P}P_x$  and  $\hat{P}S_x$  for which  $x$  indicates the depth of the discontinuity (see Aki and Richards [2002] for definition of acute accents). In addition to the problem of small relative amplitudes, the identification of  $Ps$  phases is often obscured by ambient noise and multiple reflections beneath the receiver. Therefore, specific deconvolution and stacking methods were developed to enhance the signal-to-noise ratio (SNR) of the weak  $Ps$  phase [Vinnik, 1977; Langston, 1979].

We calculate RFs in the vertical-radial coordinate system, ZRT (Z = vertical, R = horizontal radial, T = horizontal transversal) [e.g., Hannemann et al., 2016]. For the rotation into ZRT, we use the theoretical azimuth obtained using the station position and the hypocenter of the corresponding earthquake (see Table C1 in the Appendix). The  $P$  wave signal on the Z component is used to determine a time domain Wiener filter [e.g., Kind et al., 1995] which transforms the rather complex  $P$  wave signal into a band-limited spike signal. The filter is then applied to the R component to obtain the ZR RF.

For the estimation of the Wiener filter, we use the built-in function “spiking” of Seismic Handler [Berkhout, 1977; Stammer, 1993] which is able to calculate an optimum lag spiking filter [Robinson and Treitel, 1980; Yilmaz, 2008]. This function offers the possibility to use either the centroid of the signal,  $t_c$  (center of mass, equation (1)), as the spike position or a user-specified spike position. In this study, we use the centroid of the signal,  $t_c$ , as spike position, which is similar to the effective wavelet length as proposed by Berkhout [1977]:

$$t_c = \frac{\sum_{i=1}^N i \cdot |a_i|}{\sum_{i=1}^N |a_i|}. \quad (1)$$

The centroid of the signal,  $t_c$ , is calculated for a deconvolution time window containing  $N$  amplitude samples using the sample number,  $i$ , and the amplitude,  $a_i$ , of the  $i$ th sample.

The inversion to determine the Wiener filter (inverse filter) works best for minimum phase signals [e.g., Scherbaum, 2001]. As  $P$  wave signals are usually mixed phase signals, we stabilize the inversion matrix with a damping factor (0.01). The resulting RF shows several spikes representing converted phases and their multiples from different interfaces/discontinuities. The spikes of the secondary phases should be separated from the spike of the direct phase [Vinnik, 1977; Langston, 1979]. The amplitudes and delay times of the spikes of the secondary phases constrain the  $S$  wave velocity changes, their multiples the impedance contrast, and both the depths of the interfaces under investigation [e.g., Julià, 2007]. The deconvolution removes the source time function from the RFs, so that RFs from different events can be stacked after the traces have been stretched to represent time functions on a common ray path. For this distance move-out correction [Yuan et al., 1997], we use a reference distance of  $67^\circ$  and a global velocity model (oceanic PREM) [Dziewonski and Anderson, 1981].

The determination of RFs at OBSs may be influenced by water multiples [e.g., Thorwart and Dahm, 2005] or noise (tilt or water wave compliance) [e.g., Bell et al., 2015], which can be corrected on the vertical component

by using hydrophone data [e.g., *Thorwart and Dahm, 2005; Bell et al., 2015*] or the horizontal components [e.g., *Bell et al., 2015*]. We do not observe water multiples in our teleseismic recordings, and therefore, we do not apply any correction for them. Furthermore, the water wave compliance is only present at very low frequencies ( $\sim 100$  s) in 4.5–5.5 km water depth [e.g., *Crawford et al., 1998; Bell et al., 2015*]. We avoid this frequency band by high-pass filtering the RFs. The tilt noise cannot be excluded in our case and might influence the RFs at periods longer than  $\sim 10$  s. Tilting (e.g., movement of the OBS frame by currents) [*Webb, 1998; Crawford et al., 1998; Bell et al., 2015*] has a higher influence on the horizontal components than on the verticals and a correction of the vertical component [e.g., *Bell et al., 2015*] would probably lead to rather similar results for the estimated RFs [e.g., *Janiszewski and Abers, 2015*]. We therefore do not remove the tilt noise from the vertical component.

We find that the SNR of a RF is mainly determined by the quality of the earthquake recording and the length of the deconvolution time window used for the determination of the Wiener filter. To obtain RFs with sufficient SNR, we follow two approaches: (1) increase the SNR of earthquake recordings by employing “delay and sum” beamforming [*Rost and Thomas, 2002*] using either the plain recordings, or normalize the recordings to the root-mean-square (rms) amplitude of the noise ( $-200$  s to  $-100$  s before  $P$  onset) on a single component to optimize destructive interference of noise amplitudes, and (2) introduce a quality control which employs a set of evaluation criteria to select a subset of deconvolution lengths for single-station recordings and beams. A beamforming approach using OBS data is not common, and to our knowledge, our study is the first to apply this technique before the calculation of OBS RFs. We employ the normalization of the earthquake recordings to the rms amplitude of the noise on the Z component to improve the signal used for the deconvolution and on the R component to suppress the noise on the horizontal components.

To determine whether the chosen time window contains a mainly minimum phase signal or mainly noise, we choose as first evaluation criterion the spike position,  $t_{\text{rel}}$ , relative to the deconvolution time window,  $t_{\text{dec}}$ :

$$t_{\text{rel}} = \frac{t_c - \frac{t_{\text{dec}}}{2}}{t_{\text{dec}}}. \quad (2)$$

In the case of a mainly minimum phase signal, the spike position is located within the first half of the deconvolution time window ( $t_c < \frac{t_{\text{dec}}}{2} \Rightarrow t_{\text{rel}} < 0$ ). On the other hand, if the time window contains mainly noise, the spike position is in the middle of the deconvolution time window ( $t_c \approx \frac{t_{\text{dec}}}{2} \Rightarrow t_{\text{rel}} \approx 0$ ).

The success of the deconvolution is estimated by the SNR of the Z component of the RF ( $\text{SNR}_{Z/Z}$ ), which is the second evaluation criterion used. It is determined by estimating the ratio of the squared rms amplitudes in the signal time window ( $-10$  s to  $10$  s relative to  $P$  spike) and noise time window ( $-55$  s to  $-25$  s before  $P$  spike) on the Z component.

In order to quantify the success of resolving upper mantle discontinuities, the third and last evaluation criterion is the ratio of the squared rms amplitudes of the signal time window on the Z component of the RF and the noise time window on the R component of the RF ( $\text{SNR}_{Z/R}$ ). We compare this to the theoretical ratios of the refraction coefficients  $\frac{\rho \beta_{410}}{\rho \beta_{5410}}$  and  $\frac{\rho \beta_{660}}{\rho \beta_{5660}}$  assuming PREM velocities [*Dziewonski and Anderson, 1981*]. We test different deconvolution time window lengths,  $t_{\text{dec}}$ , starting with 30 s and increasing the length in 5 s steps to a time window length which approximately equals the time difference between the  $P$  onset and the  $PP$  phase arrival. The deconvolution length for each single event recording and beam is chosen by the following four steps:

1.  $t_{\text{rel}} < 0$  for mainly minimum phase signals (Figures 2a and 3a);
2.  $\text{SNR}_{Z/Z} \gtrsim 10$  for a good deconvolution (Figures 2b and 3b);
3.  $\text{SNR}_{Z/R} \gtrsim \frac{\rho \beta_{660}}{\rho \beta_{5660}}$  and/or  $\text{SNR}_{Z/R} \gtrsim \frac{\rho \beta_{410}}{\rho \beta_{5410}}$  for resolving upper mantle discontinuities (Figures 2c and 3c); and
4. manual revision of remaining RFs (Figures 2d and 3d).

The fourth step (manual revision) is required to exclude RFs which are influenced by high-frequency noise or ringing. These disturbed RFs are often hard to distinguish from undisturbed RFs with the simple evaluation criteria employed here.

We observe a small time shift in the first peak on the R component (Figure 2d) that can be explained by the influence of a sedimentary cover [*Sheehan et al., 1995*]. We calculated the mean preevent noise spectra and  $P$  wave spectra of all used events (Tables C1 and C2) using the ZRT components of the single stations

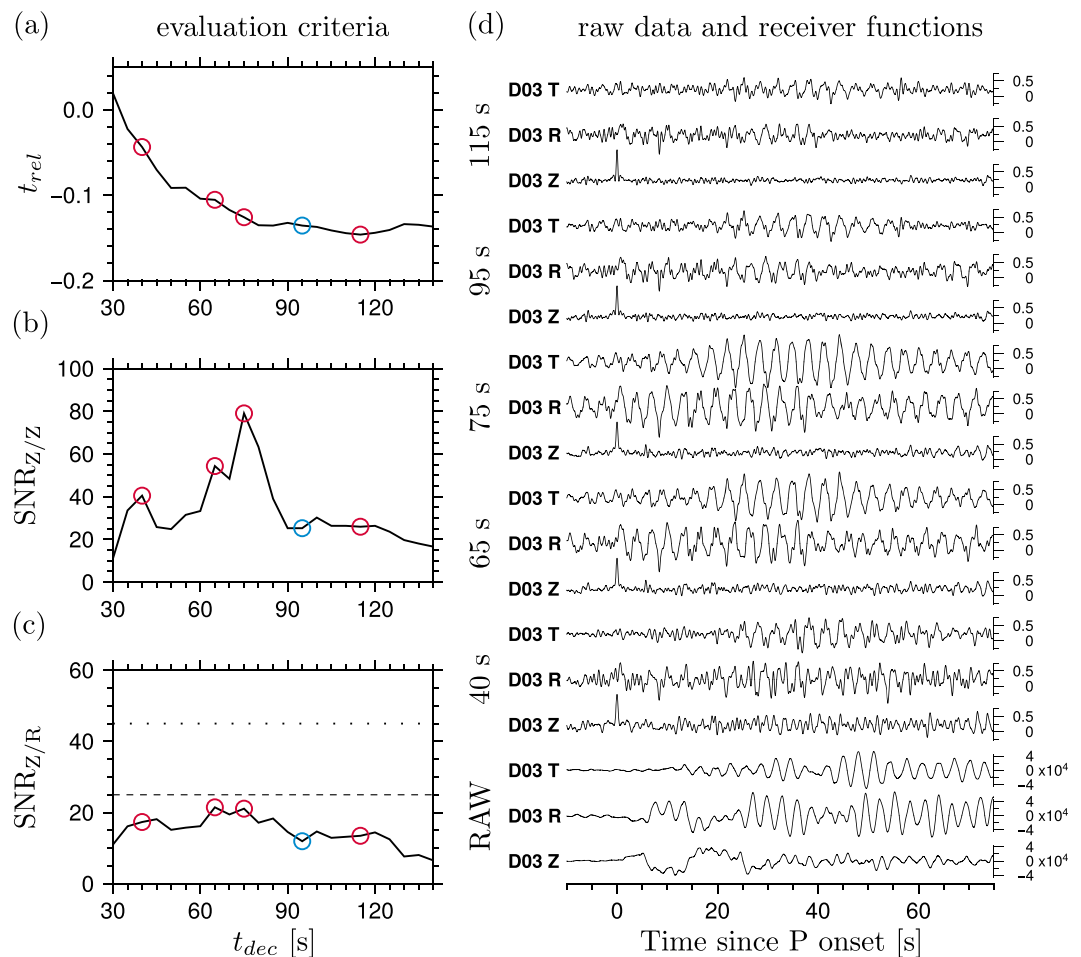


**Figure 2.** Example of the evaluation criteria shown against deconvolution time window length,  $t_{dec}$ , and preselected deconvolution time window lengths for station D03 and event #30 (Table C1 in the Appendix). The circles mark the values for the RFs presented in Figure 2d. The blue circle indicates the final chosen deconvolution length (95 s). (a) Relative spike position,  $t_{rel}$ , estimated with equation (2). (b) The SNR on the Z component. (c) The ratio of the signal time window on Z and the noise time window on R. For guidance the ratios of the refraction coefficients of the refracted P and SV waves at the 410 ( $\frac{PP_{410}}{PS_{410}}$ , dotted line) and the 660 ( $\frac{PP_{660}}{PS_{660}}$ , dashed line) are indicated. (d) The unfiltered raw data (in counts) and the RFs (normed to P spike on Z) for the different preselected deconvolution lengths (circles in Figures 2a–2c).

and the beams without normalization (Figure B1 in the appendix). The spectra show that there is often a change in spectral characteristics between preevent noise spectra and P wave spectra. Furthermore, there is evidence for sedimentary reverberations at some stations (D01–D06). Moreover, a probabilistic power spectral density analysis (PPSD) [McNamara, 2004] reveals a resonance-like effect on all three seismometer components of each station [Hannemann et al., 2016]. These effects are also visible in the raw data in Figure 2d and are probably related to signal and ambient noise-induced reverberations in the sedimentary cover at each station [Hannemann et al., 2016]. The interpretation of RFs can be hampered by the presence of such reverberations and must therefore be done carefully [Audet, 2016; Kawakatsu and Abe, 2016]. Furthermore, the ZRT coordinates are preferred for the calculation of RFs at OBSs, as the usage of the ray-oriented coordinate system (LQT) may lead to a large amplitude at 0 s on the Q component of the LQ RFs in the presence of sediment reverberations [e.g., Olugboji et al., 2016], which cannot be modeled by using a 1-D velocity-depth model.

Using the events from Tables C1 and C2 (in the Appendix), we find that beamforming improves—as expected—the  $SNR_{Z/Z}$  and the  $SNR_{Z/R}$  (Figure 3) and that this effect can be enhanced by a normalization of the individual traces before stacking (red and blue lines compared to yellow lines in Figures 3b and 3c). We get the highest  $SNR_{Z/Z}$  values of the tested normalizations for the RFs of the beams with a prenormalization

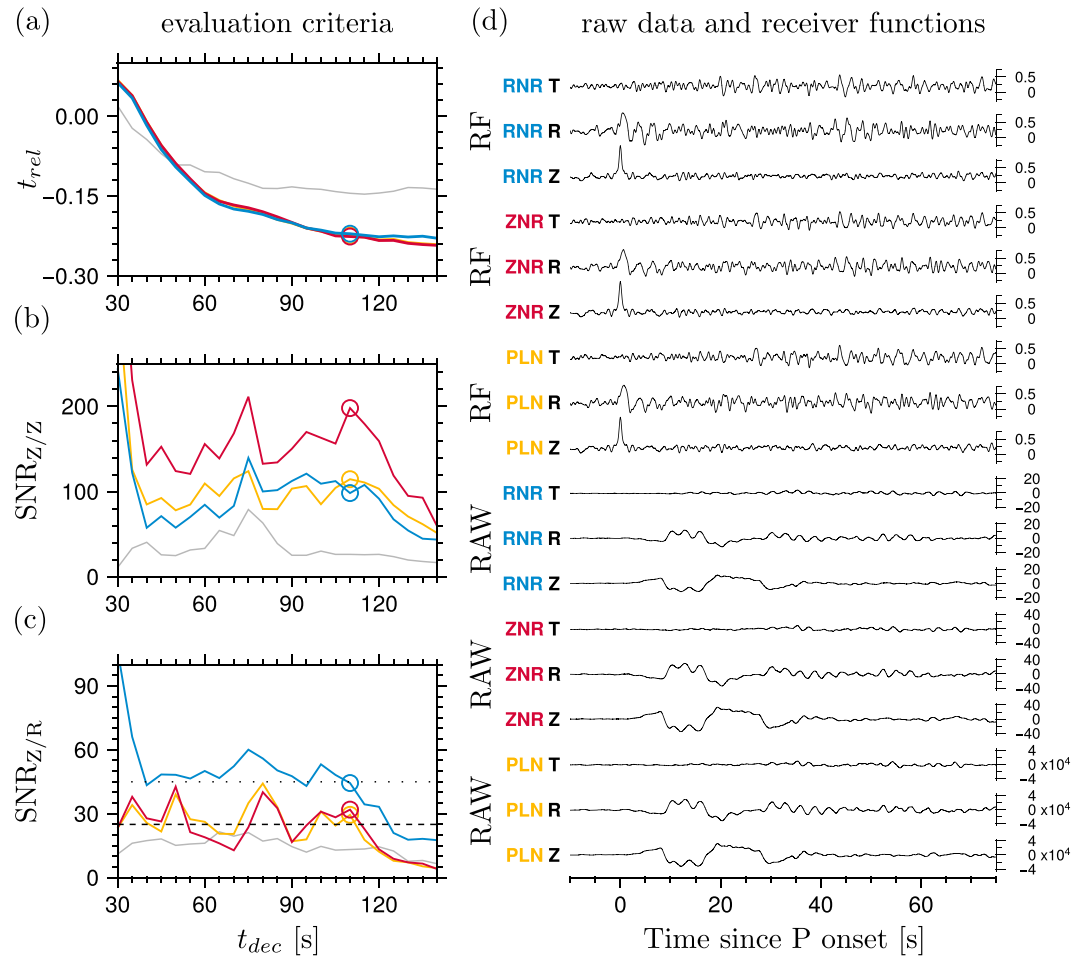


**Figure 3.** Same as Figure 2 but for traces resulting from beamforming for event #30 (Table C1 in the Appendix) and different normalization of single-station recordings (PLN, no prenormalization (yellow), ZNR, prenormalized to rms amplitude of noise on Z (red), RNR, prenormalized to rms amplitude of noise on R (blue)). The gray lines show the evaluation criteria for station D03 (Figures 2a–2c). The circles in Figures 3a–3c indicate the values for a deconvolution length of 110 s as is used for the RFs in Figure 3d.

to the rms amplitude of the noise on the Z component (ZNR). On the other hand, the highest  $SNR_{Z/R}$  of the tested normalizations is observed for the RFs of the beams with a prenormalization to the rms amplitude of the noise on the R component (RNR). We therefore present only the ZR RFs for the beams with prenormalization to the noise on either the Z or R component (ZNR or RNR) in the following analysis. Furthermore, we find that in our study 2–4 times more events are usable for the RF analysis utilizing beams than in the case of a single OBS (Table C2 in the Appendix).

For the RF analysis, we perform a bootstrap [Efron and Tibshirani, 1986] to estimate the uncertainties of the picked delay times and the confidence levels of the RF amplitudes. For this purpose, we randomly choose the RFs before stacking the distance move-out corrected traces and repeat this procedure for 300 trials [e.g., Suetsugu et al., 2010]. Furthermore, we use the amplitudes  $b_i(t)$  at time  $t$  of the total number of bootstrapped traces ( $M = 300$ ) to calculate the standard error  $\sigma(t)$  [Deuss, 2009] of the amplitude of the stacked RF  $d(t)$  at time  $t$ :

$$\sigma(t) = \sqrt{\frac{\sum_{i=1}^M [d(t) - b_i(t)]^2}{M(M - 1)}}. \quad (3)$$

We indicate the 95% confidence levels of the RFs by plotting twice the standard error  $\sigma(t)$  for the presented RF stacks. For a better visibility, we shade the areas beneath positive amplitudes in blue for which the lower confidence level is larger than zero and the areas above negative amplitudes in red for which the upper



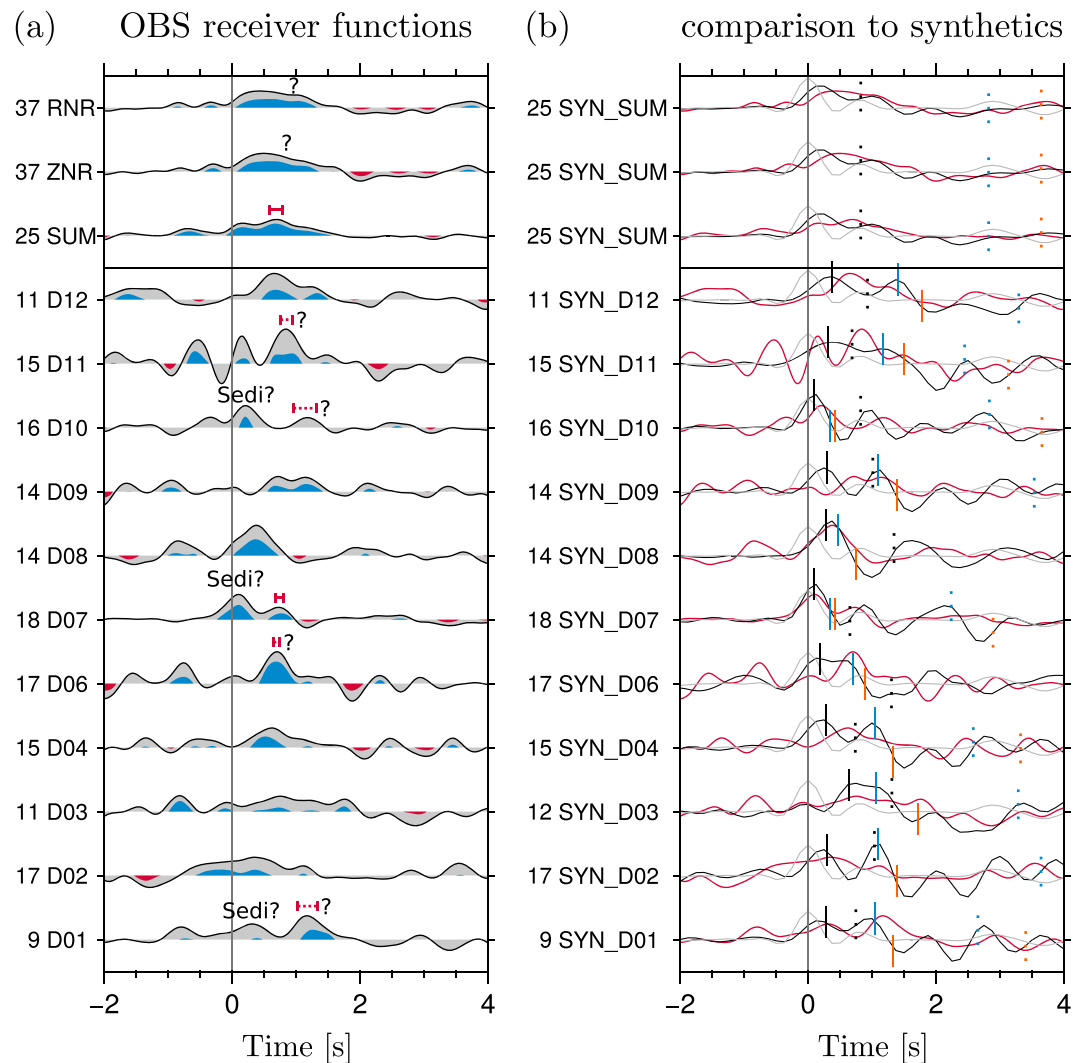


**Figure 4.** (a) Band-pass-filtered ZR receiver functions (0.5 s to 60 s). All traces have been normalized to the *P* spike on the Z component of the RFs. The colored areas show where the 95% confidence level is above zero (blue) and below zero (red) for the corresponding stations, all stations (SUM), beam-formed traces prenormalized to rms amplitude of noise on Z (ZNR) and on R (RNR). Markers indicate the positions of the Moho signal with two standard deviations estimated by picking 300 bootstrapped ZR RFs. Markers with a question mark show low confidence delay time picks. At stations D01, D07, and D10, we identify possible sediment phases. (b) Comparison of OBS RF (red, same order as in Figure 4a) to synthetic RFs calculated for models obtained by *P* wave polarization analysis (black) [Hannemann et al., 2016], and for a model with 7 km thick oceanic crust (gray). The normalized beams have not been modeled; instead, the synthetics for the all stations stack (SUM) are shown. The solid lines mark the theoretical delay times of the sediment layer and the dotted lines of the Moho. The colors represent the *Ps* (black), *PpPs* (blue), and *PpSs* (orange) phase. For the single stations, the theoretical delay times for the corresponding models by Hannemann et al. [2016] are used, and in the case of all stations and the normalized beams the theoretical Moho delay times for a 7 km thick oceanic crust are shown. The number in front of each trace indicates the number of events which contributed to the RF stacks.

confidence level is smaller than zero (e.g., Figure 4a). Since the data in our OBS network have a higher noise level compared to most land stations, such a rigorous analysis and visualization of uncertainties is very helpful for the interpretation.

#### 4. Results and Discussion

In this study, we determine the time difference between the converted (*Ps*) and the direct (*P*) phase (hereafter referred to as the delay time) on move-out corrected, stacked receiver functions (RFs) of several earthquakes.

**Table 1.** Delay Times for Selected Stations and Stack of All Stations for the Moho<sup>a</sup>

Station	D01	D06	D07	D10	D11	SUM
$t_{\text{Moho}}$ (s)	$(1.18 \pm 0.08)$	$(0.70 \pm 0.02)$	$0.74 \pm 0.03$	$(1.14 \pm 0.09)$	$(0.85 \pm 0.05)$	$0.69 \pm 0.05$

<sup>a</sup>The delay times are estimated by picking the corresponding phase on 300 stacked traces which are formed by bootstrapping the contributing ZR RF traces for each plain stack. The times are given with an error of 1 standard deviation. Estimates in brackets represent low confidence delay time picks as indicated in Figure 4a.

In the following, we discuss the observed  $P_s$  phases from different depth levels and discontinuities in the crust and upper mantle.

#### 4.1. Structure of the Oceanic Crust

In Figure 4a, we show the band-pass filtered (0.5 s to 60 s) ZR RFs for the single OBSs (D01–D12), the stack of all stations (SUM), and the stack of the beam-formed traces (ZNR and RNR). In addition, we present in Figure 4b the comparison with synthetic RFs calculated for velocity–depth models obtained by  $P$  wave polarization analysis (black) [Hannemann *et al.*, 2016] which consist of a sedimentary, a crustal and an uppermost mantle layer over PREM, and a simple model without a sediment layer and an oceanic crustal thickness of 7 km (gray). As previously stated, the time shift of the first peak on the RFs indicates the presence of a sedimentary layer and is also visible in the mismatch between the OBS RFs and the synthetics obtained for the 7 km thick oceanic crust. The presence of a sedimentary cover as estimated by Hannemann *et al.* [2016] leads to a complex interference pattern of sediment and Moho phases and multiples in the first seconds of the RFs (compare the black curves in Figure 4b). This biasing effect of a sedimentary cover often restricts the direct interpretation of OBS RFs [Audet, 2016], as discussed by Kawakatsu and Abe [2016].

In a comparison with the synthetic data (Figure 4b), we identify a positive early arrival on the ZR RFs of the stations D01, D07, and D10, and probably D08 which may be related to the sediment layer. The delay times at D01 ( $\sim 0.3$  s) and D07 ( $\sim 0.1$  s) match well with the theoretical delay times of the models obtained by Hannemann *et al.* [2016] (D01: 0.28 s, D07: 0.09 s). At station D10, the first positive amplitude arrives slightly later ( $\sim 0.2$  s) than predicted by the synthetic model (0.09 s) [Hannemann *et al.*, 2016]. This may be caused by the poorly resolved sediment layer in the model for station D10 [Hannemann *et al.*, 2016]. At station D08, the synthetic RF suggests that the first peak is likely a mixture of several phases. In general, mismatches between the synthetics calculated with the sediment models obtained by Hannemann *et al.* [2016] and the OBS data are found particularly for those stations at which the sediment model is based on only few  $P$  wave recordings, *i.e.*, in the case of stations D09 and D12.

For the identification of the Moho and the determination of its robustness, we use the information provided by the comparison of the ZR RFs with the synthetic data (Figure 4b), and the 95% confidence level. In conclusion, we find one single station within the array (D07) at which we are confident about the identified Moho (Figure 4 and Table 1). First of all, the lower confidence level identifies this peak as being robust for all bootstrapped traces. Second, the OBS RFs and the synthetic RFs have a similar appearance which indicates low influence of noise on the RFs. There is some evidence for the presence of a Moho-related signal at other single stations (D01, D06, D10, and D11, Table 1), but the comparison with the synthetic data and the estimated confidence levels indicate that these are biased by the interference with sediment related signals.

Furthermore, the ZR RF stacks of all stations provides an estimate for an average Moho delay time (0.68 s, Figure 4a and Table 1). Although the beam-formed traces ZNR and RNR show comparable amplitudes to the stack of all stations (SUM), we cannot clearly identify the Moho signal on these beam traces. This is probably related to the effect of the interference of the reverberations originating from the different sedimentary models at the individual stations in the beam-formed traces which leads to the observed broad peak in the RF beams.

We estimate theoretical  $P_s$  delay times for depth intervals of 2 km using the PREM velocity model [Dziewonski and Anderson, 1981] and a slowness of  $6.4$  s/°, which corresponds to a distance of  $67^\circ$ , which was also used for the move-out correction. Based on these values, we estimate pseudodepths using the obtained Moho delay times (Table 1). This results in depths of 4.8–5.1 km for station D07 and the stack of all stations (SUM). This crustal thickness is less than the expected values for oceanic crust [*e.g.*, White *et al.*, 1992; Laske *et al.*, 2013] and slightly less than the values obtained by Hannemann *et al.* [2016]. In addition, we marked

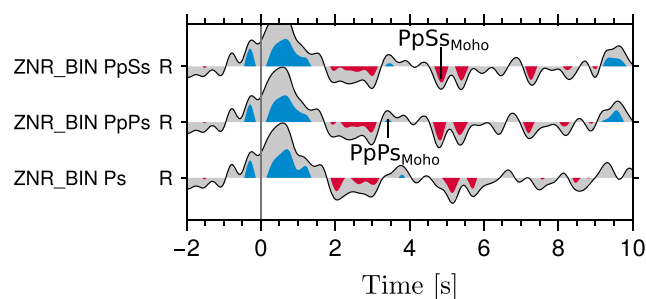


**Figure 5.** Move-out corrected and stacked ZNR RFs. ZNR RFs have been stacked in slowness bins of  $0.5 \text{ s}^\circ$  every  $0.25 \text{ s}^\circ$  before move-out correction for phases  $P_s$ ,  $PpPs$ , and  $PpSs$ , and stacking of all traces. Band pass  $0.5\text{--}60 \text{ s}$ . The RFs have been normalized to the  $P$  spike on the  $Z$  component. Markers indicate positions of possible multiples.

a possible  $PpPs$  Moho multiple at  $\sim 3.4 \text{ s}$  and a possible  $PpSs$  Moho multiple at  $\sim 4.8 \text{ s}$  on the stacks of properly time-shifted ZNR RF stacks which have been binned in the slowness domain (bins of  $0.5 \text{ s}^\circ$  every  $0.25 \text{ s}^\circ$ ) before the move-out correction (Figure 5). The delay times of these multiples correspond well to an interface at  $\sim 7\text{--}8 \text{ km}$  depth which agrees with the expected thicknesses for oceanic crust [e.g., White *et al.*, 1992; Laske *et al.*, 2013]. This indicates that the later arriving crustal multiples may be less disturbed by sediment reverberations than the direct Moho phase.

#### 4.2. Lithosphere-Asthenosphere Boundary (LAB)

In Figure 6, we present the ZR RFs filtered in two different period bands ( $2\text{--}40 \text{ s}$  in Figure 6a and  $4\text{--}40 \text{ s}$  in Figure 6b) to discuss negative phases which might be associated with the lithosphere-asthenosphere boundary (LAB). First of all, we observe an oscillation with a dominant period of  $\sim 3 \text{ s}$  at most single stations (e.g., D01–D06, D11, and D12 in Figure 6a). This is likely related to sediment and crustal reverberations and has a large influence on the overall appearance of the RFs. The RFs at the stations D07–D10 show fewer indications for the presence of strong sedimentary and crustal reverberations after  $\sim 4 \text{ s}$ . On the other hand, at station D09 we observe strong acausal amplitudes similar to stations D06 and D11. Station D09 might therefore also be problematic for the further analysis of possible LAB phases. At stations D07, D08, and D10, we observe small negative phases at  $\sim 8 \text{ s}$  for the filter band between  $2 \text{ s}$  and  $40 \text{ s}$  which tend to merge with the neighboring phases for the filter band between  $4 \text{ s}$  and  $40 \text{ s}$ . A negative phase at  $\sim 8 \text{ s}$  is also visible at stations D02, D03, D04, and D06, but at these stations it is likely related to the strong sediment and crustal reverberations. In the stack of all stations (SUM) and the normalized beam traces (ZNR and RNR), we observe negative phases at  $\sim 5 \text{ s}$  and  $\sim 8 \text{ s}$  indicated by faint green areas in Figure 6. The phase at  $\sim 5 \text{ s}$  is likely related to the  $PpPs$  multiple of the Moho (Figure 5) and the phase at  $\sim 8 \text{ s}$  is probably a combination of the already discussed reverberations at most of the stations and the negative phase at similar times observed at stations D07, D08, and D10. If these phases were related to discontinuities in the subsurface, the delay times would correspond to interfaces at depths of  $40\text{--}50 \text{ km}$  ( $\sim 5 \text{ s}$ ) and  $65\text{--}75 \text{ km}$  ( $\sim 8 \text{ s}$ ).

Figure B2 (in the Appendix) shows stacks of all single station RFs, which have been stacked in  $0.5 \text{ s}^\circ$  slowness bins, depending on their slowness. Furthermore, we indicate the delay times of an interface at  $40\text{--}50 \text{ km}$  depth (light green area in Figure B2 in the Appendix) and at  $65\text{--}75 \text{ km}$  depth (dark green area in Figure B2 in the Appendix) assuming PREM [Dziewonski and Anderson, 1981]. A clear move-out is not observable for the negative phase at  $\sim 5 \text{ s}$ , but might be possible for the phase at  $\sim 8 \text{ s}$ , although we observe several multiples arriving at similar times (e.g., for slowness  $4\text{--}5 \text{ s}^\circ$  at  $\sim 8\text{--}9 \text{ s}$ ). These multiples are probably related to sedimentary and crustal structures. Just based on this slowness bin stack, we cannot determine whether one of the negative phases at  $\sim 5 \text{ s}$  and  $\sim 8 \text{ s}$  is related to the LAB.

We model synthetic ZR RFs for different LAB depths (Figure 7) to further investigate the interference of the sedimentary and crustal multiples and a sharp LAB (velocity drop of  $\sim 11.3\%$  from  $v_s = 4.51 \text{ km/s}$  to  $v_s = 4 \text{ km/s}$ ). The models obtained by  $P$  wave polarization [Hannemann *et al.*, 2016] have been used for the upper  $10.5 \text{ km}$ . From depths of  $10.5 \text{ km}$  to  $20.5 \text{ km}$ , we use a gradient from the uppermost mantle velocities in the corresponding model, to “normal” mantle velocities ( $v_p = 8.12 \text{ km/s}$ ,  $v_s = 4.51 \text{ km/s}$ ). We use the same station and event distribution as for the OBS data. In Figures 7a and 7b, we compare the stack of all stations (SUM) and the normalized beams (ZNR and RNR) with a stack of all synthetic RFs (SYN\_SUM) for different LAB depths (black:  $30 \text{ km}$ , red:  $50 \text{ km}$ , blue:  $70 \text{ km}$ , and green:  $90 \text{ km}$ ). The synthetics show a similar influence of the sediment and crustal reverberations on the overall appearance of the RFs as the OBS data. Furthermore, the effect of the LAB at different depths on the RFs is often only identifiable by the direct comparison with the other models (e.g., LAB at  $30 \text{ km}$  depth for band pass  $2\text{--}40 \text{ s}$ , Figure 7a) due to the interference with the sediment and crustal reverberations. The LAB signal in the stack of all stations is therefore masked by the influence

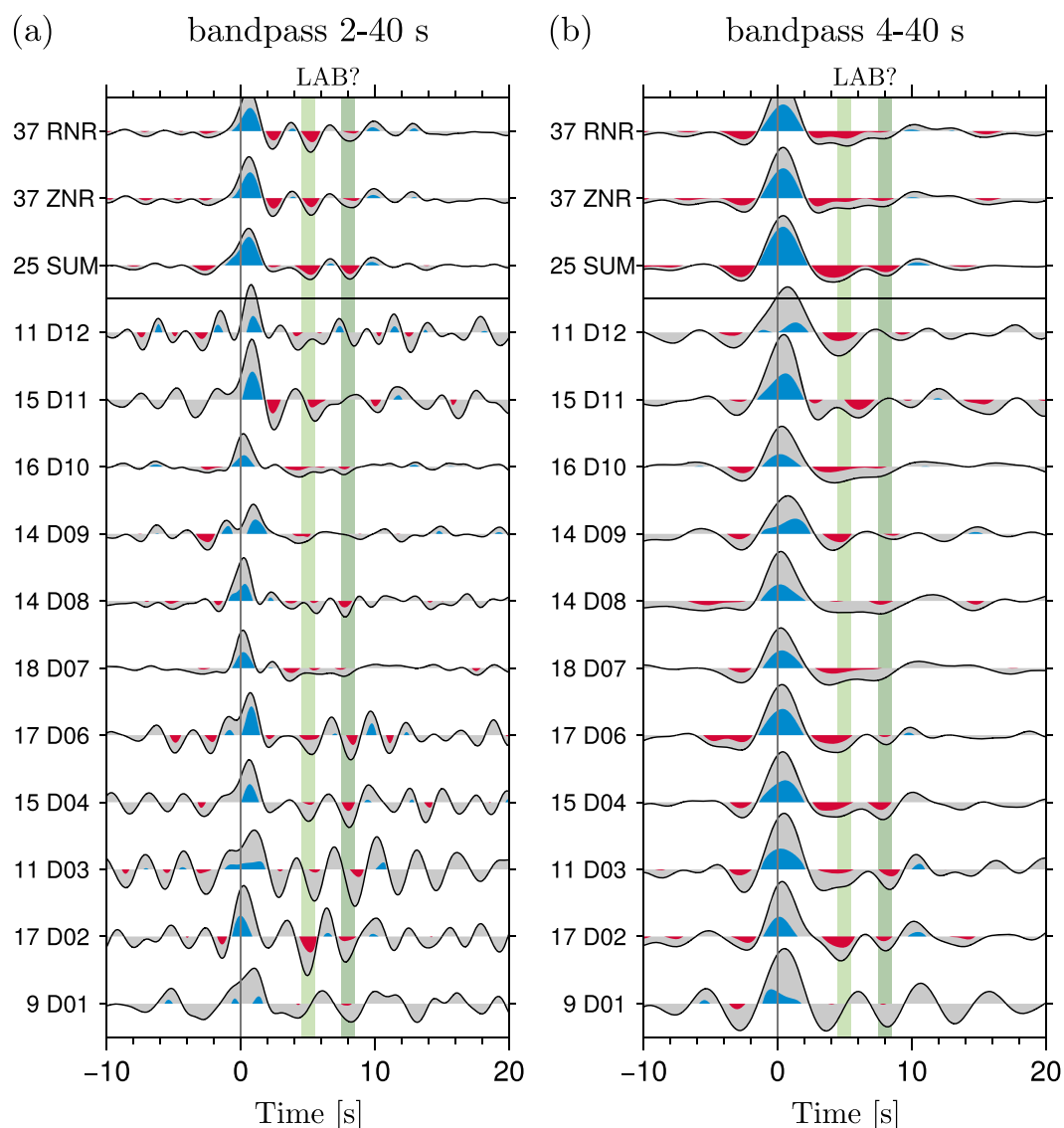


**Figure 6.** Band-pass-filtered ZR receiver functions ((a) 2 s to 40 s and (b) 4 s to 40 s). The colored areas show where the 95% confidence level is above zero (blue) and below zero (red) for the single stations, all stations (SUM), beam-formed traces prenormalized to rms amplitude of noise on Z (ZNR) and beam-formed traces prenormalized to rms amplitude of noise on R (RNR). The faint green areas indicate the arrivals of phases probably related to the lithosphere-asthenosphere boundary (LAB) at  $\sim 5$  s and  $\sim 8$  s. The number in front of each trace indicates the number of events which contributed to the RF stacks. All traces have been normalized to the  $P$  spike on the Z component.

of the different sedimentary and crustal structures at the single stations. A quantitative modeling of LAB depth and velocity reduction at the LAB would first of all require an in-depth analysis of the sedimentary and crustal structure at the single stations, in order to properly model the sediment and crustal reverberations. The stack of the current synthetics shows a time shift in the first peak compared to the real data, which indicates that the models probably underestimate the sediment effect. Furthermore, we notice that during the modeling done so far, not all effects of the sedimentary and crustal structure which are observed at the OBSs can be modeled with 1-D velocity-depth models (e.g., the aforementioned resonance). Based on our experiences with data quality and modeling effort, the ability of detailed quantitative modeling to capture the sediment and crustal reverberations remains unclear and such modeling is therefore beyond the scope of this study. We have to conclude from Figures 7a and 7b that we are not able to give a depth estimate for the LAB for the whole working area by using the stacks of all stations and the normalized beams.

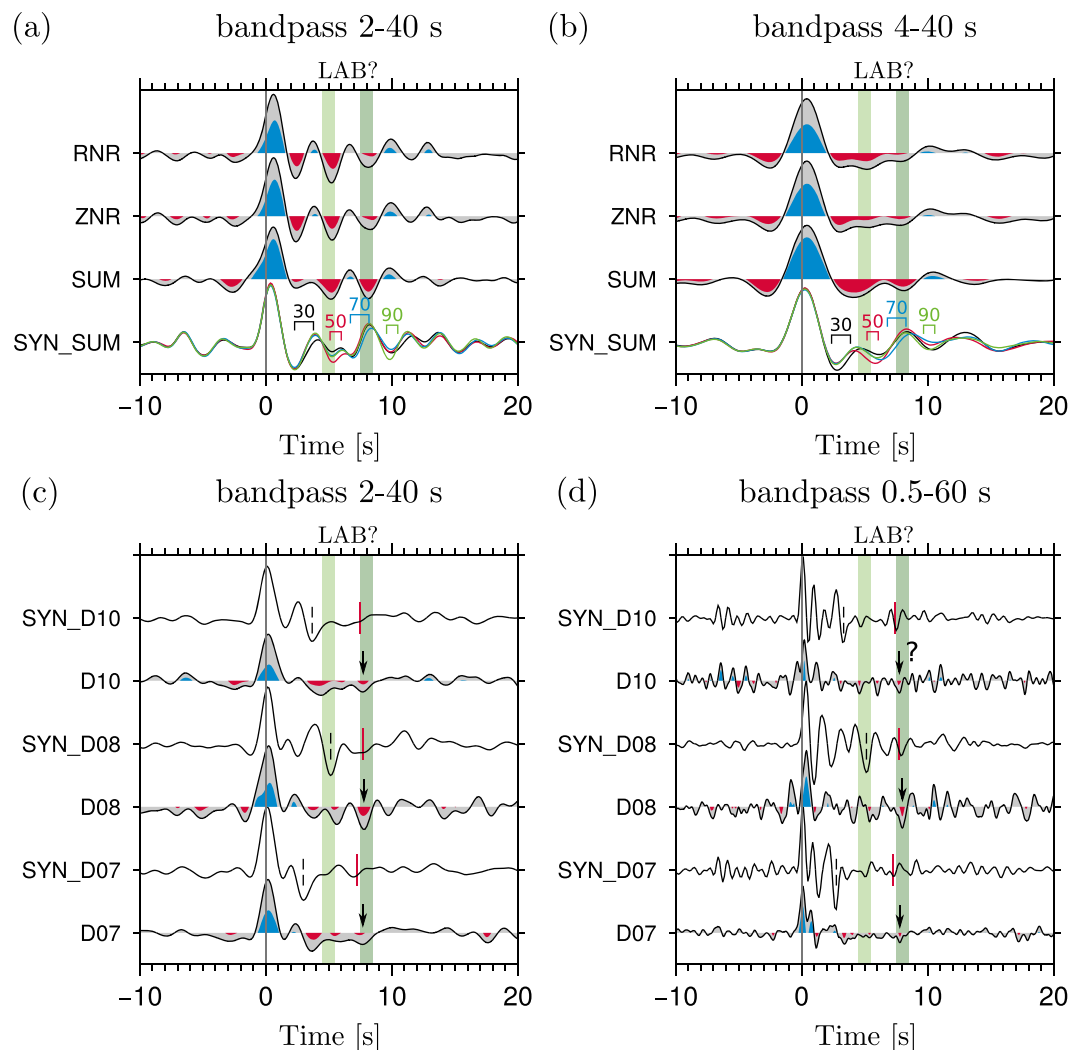


**Figure 7.** Comparison between synthetic ZR RFs using the models obtained by *Hannemann et al.* [2016] (black lines in Figure 4b) and OBS data. The colored areas show where the 95% confidence level is above zero (blue) and below zero (red) for the single stations, the stack of all stations (SUM), beam-formed traces prenormalized to rms amplitude of noise on Z (ZNR) and beam-formed traces prenormalized to rms amplitude of noise on R (RNR). The faint green areas indicate the arrivals of phases probably related to the LAB. (a, b) Comparison between synthetics (SYN\_SUM) and SUM, ZNR and RNR. The line colors of the synthetic RFs indicate the depths of the LAB in the used models (black: 30 km, red: 50 km, blue: 70 km, green: 90 km). The markers indicate the identified arrival of the LAB phase in the synthetics. The RFs have been band-pass filtered (2–40 s (Figure 7a) and 4–40 s (Figure 7b)). (c, d) Comparison of ZR RFs of single stations (D07, D08, and D10) with corresponding synthetics (SYN\_D07, SYN\_D08, and SYN\_D10) for models with an LAB at 70 km depth. Black arrows indicate probable LAB phases. Black dashed markers indicate arrival of *PpPs* Moho multiple and red markers of LAB phases on the synthetic traces. The delay times have been calculated based on the corresponding velocity-depth model for each station. The RFs have been bandpass filtered (0.5–60 s (Figure 7c) and 2–40 s (Figure 7d)). All RFs have been normalized to the *P* spike on the Z component.

Nevertheless, the single stations D07, D08, and D10—as was already pointed out—are less influenced by strong sedimentary and crustal reverberations, which is also visible in the *P* wave spectra (Figures B1f, B1g and B1i in the Appendix). From the *P* wave polarization analysis [*Hannemann et al.*, 2016], we know that the sediments are rather thin (300–400 m) at these stations. Most of the sediment and crustal multiples therefore arrive before ~4 s (Figure 4b) and do not interfere with the later arriving negative phase at ~8 s. Furthermore, the comparison between the synthetics and the OBS RFs in Figure 4 (band pass 0.5–60 s) showed that they agree quite well in the first seconds at stations D07, D08, and D10. In Figure 7c, we observe that the shapes of synthetics for an LAB at 70 km and the real data are comparable in the first seconds for the filter band between 2 s and 40 s. The synthetics also show that the *PpPs* multiple of the Moho is a much stronger negative phase

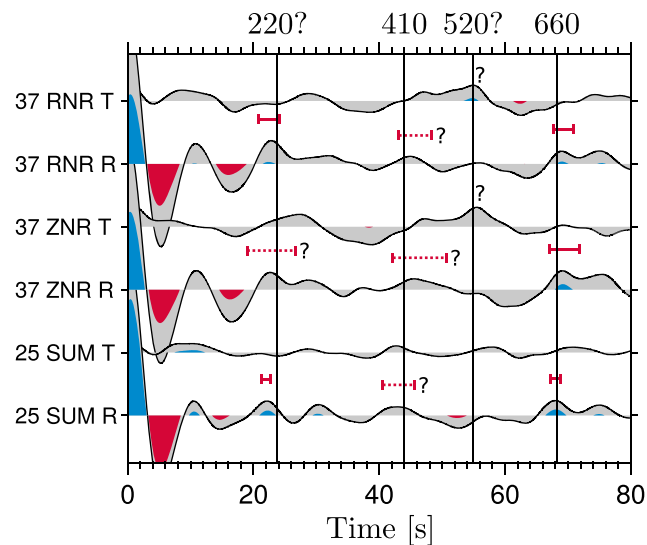


**Figure 8.** Band-pass filtered ZR receiver functions (7 s to 60 s). The colored areas indicate where the 95% confidence level is above zero (blue) and below zero (red) for the RF stacks (all stations: SUM; beam-formed traces prenormalized to the rms amplitude of noise on Z: ZNR; beam-formed traces prenormalized to the rms amplitude of noise on R: RNR). The markers indicate the position of the signals corresponding to the 410, the 660, and the probable signals of the Lehmann discontinuity (220) with 2 standard deviations estimated by picking 300 bootstrapped RFs. The RFs have been normalized to the  $P$  spike on the Z component. Solid lines show the delay times corresponding to depths of 220 km, 410 km, 520 km, and 660 km assuming PREM [Dziewonski and Anderson, 1981]. The number in front of each trace indicates the number of events which contributed to the RF stack.

at  $\sim 3\text{--}5$  s, in comparison to the later arriving LAB phase ( $\sim 7\text{--}7.5$  s). Furthermore, the LAB phase is hard to identify in this filter band due to the interference with other multiples. For shorter periods (band pass 0.5–60 s, Figure 7d), we can identify small negative phases at  $\sim 8$  s at D07, D08, and D10, although the phase at D10 remains questionable due to similar earlier negative phases. Nevertheless, we have to be aware that at these short periods we are approaching the limits of resolution of our data; therefore, we have to be careful with interpreting the observations. The observed phases at  $\sim 8$  s (marked by black arrows in Figures 7c and 7d) arrive a bit later than the LAB phases in the corresponding synthetic RFs and indicate a probable sharp LAB. Their delay times correspond to LAB depths between 70 km and 80 km if the sediment and crustal structure obtained by  $P$  wave polarization is assumed at the single stations. For a lithospheric age between 75 Ma and 85 Ma as in this study (Figure 9) [after Müller *et al.*, 2008], the observation of an LAB in 70–80 km depth would be in line with depth observations made for similar ages in the Pacific [Rychert *et al.*, 2012, Figure 6].

In summary, we conclude that there might be a probable sharp LAB at  $\sim 70\text{--}80$  km, for which we find weak evidence at single stations with rather thin sediments (300–400 m). Furthermore, we notice that strong sedimentary and crustal reverberations mask the arrival of the LAB phase and need to be considered in the discussion or modeling of potential LAB phases.

#### 4.3. Upper Mantle Discontinuities

The  $P$ s converted phases caused by the 410 and 660 should arrive  $\sim 44$  s and  $\sim 68$  s after the direct  $P$  phase and have positive amplitudes. These amplitudes are several tens of times smaller than the direct  $P$  phase (compare  $\frac{PP_{410}}{PS_{410}}$  and  $\frac{PP_{660}}{PS_{660}}$  in Figure 2c). The usual approach to enhance them is stacking. In Figure 8, we present the band-pass filtered (7–60 s) stacked ZR RFs of the single stations (SUM) and beam-formed traces with different prenormalizations (ZNR and RNR). The delay times shown as guidance correspond to depths of 220 km, 410 km, 520 km, and 660 km assuming PREM [Dziewonski and Anderson, 1981]. For the upper mantle, we can clearly identify one positive phase at  $\sim 68\text{--}69$  s (Table 2) and a second low-confidence phase at  $\sim 43\text{--}46$  s (Table 2). We associate the phase at  $\sim 43\text{--}46$  s with the 410 and the phase at  $\sim 68\text{--}69$  s with the 660.

The expected delay time for the 410 assuming PREM velocities is 43.97 s, which agrees quite well with the measured delay times of the stacks of the single stations ( $43.11 \pm 1.26$  s) and is similar to the measured delay times of the beam-formed traces (ZNR:  $46.46 \pm 2.13$  s, RNR:  $45.76 \pm 1.31$  s). This indicates a normal depth of the 410, which is in good agreement with observations made by Saki *et al.* [2015] in their precursor study. The expected delay time for the 660 assuming PREM is 68.26 s. The measured delay times are similar (SUM:  $68.01 \pm 0.41$  s, ZNR:  $69.46 \pm 1.18$  s, and RNR:  $69.26 \pm 0.78$  s). Although Saki *et al.* [2015] provide only a few depth estimates for the 660, our observations match their  $PP$  precursor estimates north and south of our OBS array. Transforming delay times of the mantle discontinuities to pseudodepths is usually strongly influenced by the velocity model of the uppermost mantle and crust. It is therefore common practice to employ more robust

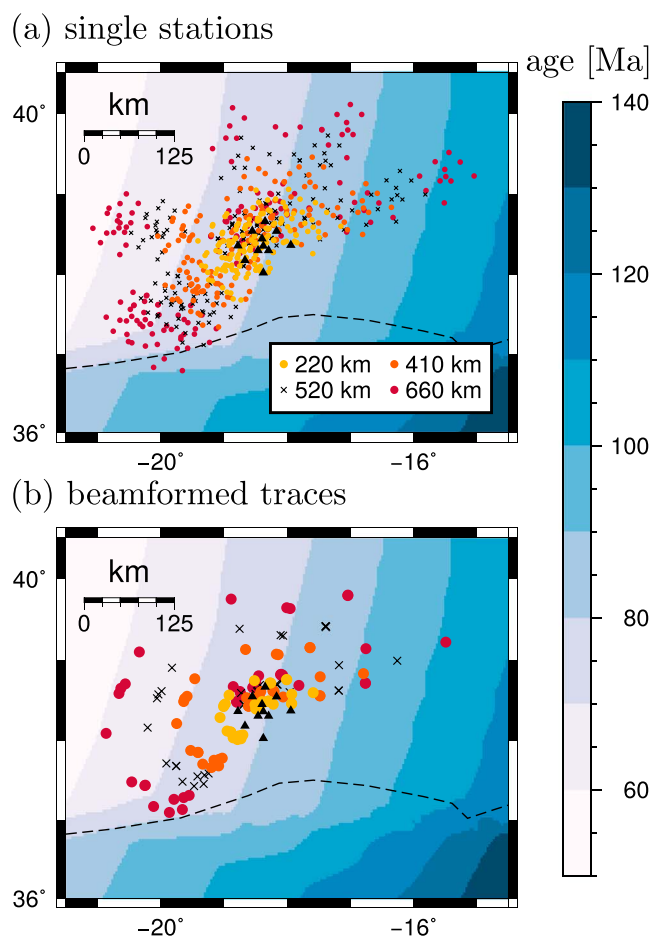


**Figure 9.** Location of piercing points of upper mantle discontinuities for (a) single stations and (b) beam-formed traces (estimated for the center of the array). The age of the oceanic lithosphere in million years [Müller *et al.*, 2008] is shown by the color shading. The piercing points are shown for depths of 220 km (yellow circles, Lehmann discontinuity), 410 km (orange circles), 520 km (black crosses), and 660 km (red circles). The locations of the OBSs used are indicated as black triangles. The position of the Eurasian-African plate boundary (Gloria Fault) [Bird, 2003] is marked as a black dashed line.

estimates like the delay time difference between the 660 and the 410 [e.g., Gu and Dziewonski, 2002]. This difference is  $24.9 \pm 1.33$  s (Table 2) for the single station stack (SUM),  $23.00 \pm 2.44$  s (Table 2) for the stack of the beam-formed traces normalized to the noise on the Z component (ZNR), and  $23.50 \pm 1.52$  s (Table 2) for the stack of the beam-formed traces normalized to the noise on the R component (RNR). This difference between the 410 and the 660 is similar to the theoretical estimate using PREM (24.29 s) within the error bounds.

A small time shift of the MTZ *Ps* phases can be observed ( $\sim 1.5$  s, Table 2) between the single stations' stack and the stack of the beam-formed traces. We investigate whether this observed time shift of the 410 and 660 is related to the different processing of the single stations and the beam-formed traces by calculating synthetic RFs using a full wave field reflectivity method (QSEIS) [Wang, 1999] with our station distribution, a global velocity model (PREM) [Dziewonski and Anderson, 1981] and a local crustal model (CRUST1.0) [Laske *et al.*, 2013]. We find no difference in the estimated delay times of the mantle discontinuities for the beam-formed traces stack and the stack of the single stations. The small time shift in the delay times between the single stations stack and the beam-formed traces stack (Figure 8) may therefore indicate a difference in the velocities or the thicknesses of the lithosphere and mantle above the 410 sampled by the according rays.

Examining the map showing the piercing points (Figure 9), we find that the RFs mostly sample structures within the Eurasian plate (north of the Gloria Fault) for back azimuths between  $\sim 200^\circ$  and  $80^\circ$ . The azimuthal coverage is similar for the single stations and the beam-formed traces. It is therefore likely that the small time shift between the different stacks is caused by the method-specific differences in the weighting according to the noise (i.e., the prenormalization to the rms amplitude of the noise).

**Table 2.** Delay Times for Stacked Traces and Beam-Formed Traces for Lehmann (220), "410," and "660" Discontinuities<sup>a</sup>

Station	$t_{220(?)}$ (s)	$t_{410}$ (s)	$t_{660}$ (s)
SUM	$21.96 \pm 0.35$	$(43.11 \pm 1.26)$	$68.01 \pm 0.41$
ZNR	$(22.84 \pm 1.92)$	$(46.46 \pm 2.13)$	$69.46 \pm 1.18$
RNR	$22.46 \pm 0.82$	$(45.76 \pm 1.31)$	$69.26 \pm 0.78$
PREM	23.81	43.97	68.26

<sup>a</sup>The times are estimated by picking the corresponding phase on 300 stacked traces which were formed by bootstrapping the contributing traces. The times are given with an error of 1 standard deviation. Estimates in brackets represent low confidence delay time picks as indicated in Figure 8.

There is another low-confidence signal at a delay time of  $\sim 22$ – $23$  s (Figure 4 and Table 2). This signal arrives slightly earlier than would be expected for a depth of 220 km in PREM (23.81 s, Figure 8). The association of this phase with the Lehmann discontinuity is difficult, as it has a low confidence level and likely interferes with crustal and lithospheric multiples (see first 20 s in Figures 6a, 6b, and 8).

In addition, a low-confidence, weak signal is visible at  $\sim 56$  s on the T components of the beam-formed traces, the arrival of which is delayed compared to the expected arrival of the "520" from PREM (54.92 s, see Figure 8). Onsets on the T component of RFs can be caused by dipping layers or shear wave splitting in anisotropic layers [e.g., Cassidy, 1992; Savage, 1998; Farra and Vinnik, 2000]. The oceanic upper mantle is anisotropic in global models like PREM and shows lateral and depth-dependent variations of anisotropy in surface wave-based tomography models [Piliidou *et al.*, 2005]. However, it is hard to identify signals on the R component (Figure 8) which might represent a split shear wave component near the T component signal at  $\sim 56$  s. If this signal originates due to anisotropy in a layer above 520 km depth, shear waves converted at 660 km depth should be split as well. This is not observable in Figure 8. The limited number of available RFs, as well as their often low signal quality hinder the formation of back azimuth-dependent stacks with a sufficient confidence level. The latter would be required to constrain a possible anisotropy component in the data. The cause of this signal therefore remains enigmatic.

In summary, the usage of beamforming techniques increases the number of events available for the RF analysis and therefore also the SNR of the RF. In combination with bootstrapping and uncertainty estimations, they help to estimate the confidence of signals originating from deeper mantle structures as the MTZ.

## 5. Conclusion

This study shows that it is possible to identify discontinuities in the oceanic crust and upper mantle down to the MTZ using OBS data. Furthermore, it explores the advantages of using beamforming to improve the signal quality of RFs and a quality control employing evaluation criteria such as relative spike position and SNR to search for the optimal deconvolution length. In this study, we demonstrate that these techniques work well.

The first analyzed discontinuity is the Moho, for which the average pseudodepth is  $\sim 5$  km estimated using PREM velocities. This is slightly less than would be expected for oceanic crust in general [e.g., White *et al.*, 1992; Laske *et al.*, 2013]. The RFs show evidence for the presence of a sediment layer at the single stations which likely influences the estimated delay times and therefore the pseudodepths. Furthermore, possible crustal multiples indicate a Moho depth of  $\sim 7$ – $8$  km which is more in line with the expected values [e.g., White *et al.*, 1992; Laske *et al.*, 2013].

Second, we focus on the asthenosphere. The interpretation of the LAB and the Lehmann discontinuity is difficult because of simultaneously arriving reverberations of sediment, crustal, and lithospheric structures and requires synthetic modeling to understand the observed effects. The synthetic modeling indicates that the influence of sedimentary and crustal reverberations masks the arrival of the LAB phase for the stack of all stations and the normalized beams. Nevertheless, at single stations with thin (300–400 m) sediments, a weak negative phase indicates a probable sharp LAB at  $\sim 70$ – $80$  km depth. These estimates are in line with depth estimates for similar ages in the Pacific [Rychert *et al.*, 2012]. A positive phase arrival at  $\sim 22$ – $23$  s on the RF stacks may correspond to the Lehmann discontinuity [e.g., Deuss *et al.*, 2013] but likely interferes with crustal and lithospheric multiples.



We find that the 410 and the 660 are located at depths expected from PREM and are in line with a recent precursor study in this area [Saki et al., 2015]. A delay between the 410 and the 660 signal observed at the single stations stack and the beam-formed traces stack is likely caused by the different prenormalization of the data before the RF calculation.

In conclusion, this study shows that the number of usable events for RF studies at the ocean bottom can be more than doubled in comparison to single station approaches using beamforming techniques at a midaperture array. This approach is especially promising if deeper mantle features with small amplitudes are to be investigated as it increases the SNR of the event recordings and the number of usable events for the analysis of OBS RFs. The application of evaluation criteria supports the selection of optimal deconvolution time window lengths. Nevertheless, a manual revision of the RFs resulting from the preselected deconvolution lengths is still necessary to exclude RFs from the analysis that are influenced by high-frequency noise. Furthermore, this study proves that the combination of single OBSs and beamforming techniques gives the opportunity to investigate structures from the sea floor down to the MTZ. The analysis of the local *S* wave velocity structure via *P* wave polarization [Hannemann et al., 2016] proves to be useful in understanding the effects encountered by sedimentary and crustal reverberations at single OBSs using synthetic modeling.

### Appendix A: Orientation

We test two different approaches to estimate the orientation of the OBSs (i.e., angle between geographic north and the north component of the seismometer): (1) using the *P* wave polarization on the horizontal components, and (2) using the phase shift of the Rayleigh wave between the vertical and radial components. For the analysis of the *P* wave polarization, we measure the amplitudes of several teleseismic *P* phases on all three components for each station. We estimate the theoretical amplitude distribution of the *P* phase on the horizontal components by using the vertical *P* wave polarization and the known back azimuth of the earthquake. After a stepwise rotation of the theoretical amplitude distribution, we calculate the difference (misfit) between the theoretical and the measured horizontal amplitudes.

We estimate this misfit for several events and calculate the mean and standard deviation. We use the definitions of mean,  $\mu$ , and standard deviation,  $\sigma$ , from directional statistics analogous to Grigoli et al. [2012] for *N* measurements of the orientation angle,  $\varphi_i$ , with weight  $w_i$ , which is chosen based on event quality.

$$\mu = \arctan\left(\frac{Q}{P}\right) \wedge \sigma = \sqrt{2 \cdot (1 - R)}$$

$$\text{with } P = \sum_{i=1}^N w_i \cos \varphi_i \wedge Q = \sum_{i=1}^N w_i \sin \varphi_i \tag{A1}$$

$$\text{and } R = \frac{1}{\sum_{i=1}^N w_i} \sqrt{P^2 + Q^2}$$

Furthermore, we combine the misfit functions of all events by calculating the mean of the different misfit functions for each tested angle.

**Table A1.** Results of Orientation of OBSs (i.e., Angle Between Geographic North and the North Component of the Seismometer) Using the *P* Phase<sup>a</sup>

Station	No. of Events	Single Events	All Events	Bootstrap
D01	9	144.8° ± 27.6°	144°	144.2° ± 5.3°
D02	8	195.5° ± 17.5°	198°	198.5° ± 3.5°
D03	13	177.2° ± 34.2°	175°	175.5° ± 2.3°
D04	7	94.1° ± 28.9°	98°	99.5° ± 7.3°
D06	15	56.1° ± 49.0°	57°	57.8° ± 5.2°
D07	14	203.3° ± 32.8°	202°	202.1° ± 2.8°
D08	7	239.4° ± 31.1°	228°	233.9° ± 10.6°
D09	12	142.4° ± 32.8°	139°	141.7° ± 7.1°
D10	11	271.1° ± 51.3°	261°	262.6° ± 5.4°
D11	11	349.6° ± 34.2°	351°	351.4° ± 2.9°
D12	11	289.7° ± 53.9°	300°	298.3° ± 7.1°

<sup>a</sup>We present the results of the analysis of single events, the combined misfit function and the bootstrap. The mean and standard deviation are calculated using equation (A1).

**Table A2.** Results of Orientation of OBSs (i.e., Angle Between Geographic North and the North Component of the Seismometer) Using the Rayleigh Phase<sup>a</sup>

Station	No. of Events	Single Events	All Events	Bootstrap
D01	24	140.3° ± 13.7°	142°	140.4° ± 2.2°
D02	28	193.7° ± 13.0°	195°	193.1° ± 2.3°
D03	28	164.9° ± 12.9°	166°	164.5° ± 2.2°
D04	27	99.1° ± 17.4°	98°	96.8° ± 2.2°
D06	25	48.5° ± 25.7°	49°	48.0° ± 2.5°
D07	20	197.9° ± 8.9°	197°	196.9° ± 1.8°
D08	18	226.2° ± 11.1°	228°	225.8° ± 2.6°
D09	21	138.6° ± 8.0°	137°	136.6° ± 2.2°
D10	11	252.2° ± 13.9°	254°	251.2° ± 3.0°
D11	18	349.2° ± 10.5°	349°	348.5° ± 2.9°
D12	21	299.7° ± 15.5°	300°	300.2° ± 3.1°

<sup>a</sup>We present the results of the analysis of single events, the correlation coefficient of the concatenated data, and the bootstrap. The mean and standard deviation are calculated using equation (A1).

We also use surface waves to estimate the orientation of the stations [Stachnik *et al.*, 2012]. The data are filtered with a band pass between 20 and 60 s and the horizontal components are rotated using the back azimuth of the events. If the horizontal components are properly oriented, the vertical trace will be identical to the Hilbert transform of the radial trace within the time window of the Rayleigh phase [Stachnik *et al.*, 2012]. We decide to include the Love phase in our analysis, because its energy should completely vanish from the radial component if the components have the correct orientation. We use a normalized zero-lag cross correlation,  $S_{rz}$ , between the Hilbert transform of the radial trace ( $\tilde{R}$ ) and the vertical trace ( $Z$ ) (equation (A2) [Stachnik *et al.*, 2012; *Zha et al.*, 2013]).

$$S_{rz} = \frac{\rho(\tilde{R}, Z)}{\rho(Z, Z)} \quad \text{with} \quad \rho(X, Y) = \int_{t_1}^{t_2} X(t)Y(t)dt \quad (A2)$$

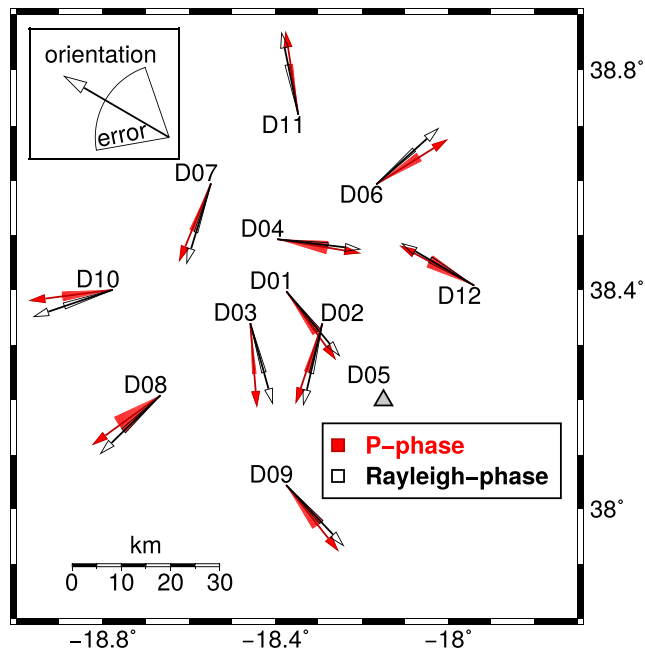


**Figure A1.** Estimated orientation of OBSs by *P* phase polarization (red arrows and slices) and Rayleigh wave ellipticity (black arrows and open slices). The arrows show the estimated directions of the north component of the seismometer and the slices the error of the orientation (see also Tables A1 and A2).

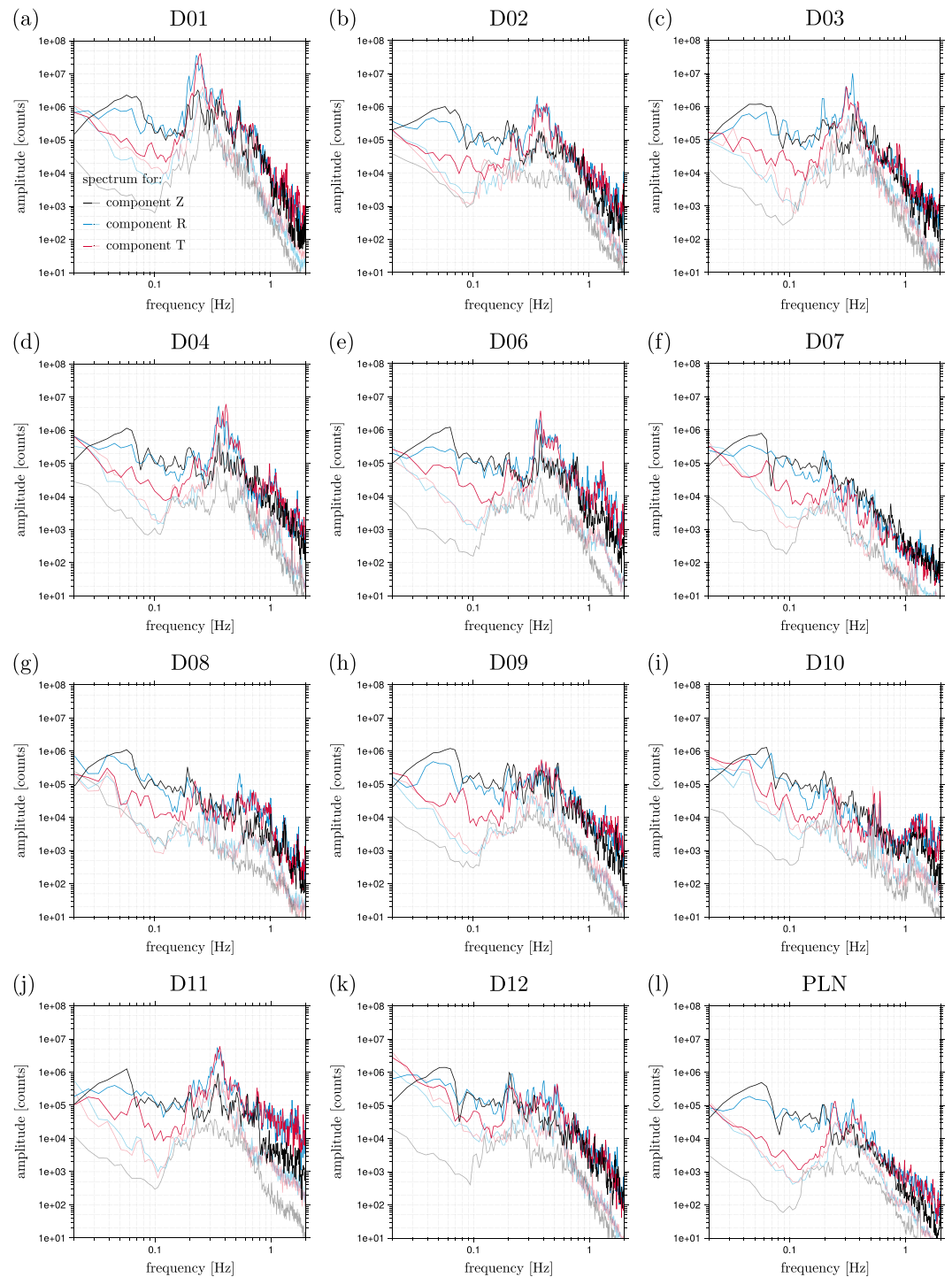


**Figure B1.** Mean spectra for all events used at the single stations (D01–D12) and for the unnormalized beam traces (PLN) (Tables C1 and C2) in the Appendix. Spectra for vertical (Z, black), radial (R, blue), and transversal (T, red) recordings of *P* waves were calculated for 200 s long seismograms starting 50 s before the *P* wave arrival. Additionally, the lighter colors show the mean spectra of the preevent noise which were calculated for a 200 s long time window starting 250 s before the *P* wave arrival.

Herein,  $\rho(\hat{R}, Z)$  is the zero-lag cross correlation between the Hilbert transform of the radial trace and the vertical trace and  $\rho(Z, Z)$  is the zero-lag autocorrelation of the vertical trace. Before calculating  $S_{rz}$ , we normalize the traces. The horizontal traces are equally treated to preserve the particle polarization. Afterward, we rotate the horizontal traces in  $1^\circ$  steps and calculate  $S_{rz}$ . As for the *P* phase, we estimate  $S_{rz}$  for several events

and calculate the mean and standard deviation according to equation (A1). Furthermore, we append all event data and process them together.

Moreover, we use the bootstrap method and equation (A1) to estimate mean and standard deviation for the combined misfit function for the *P* phase and the correlation coefficient for the Rayleigh phase. The resulting angles are presented in Table A1 for the *P* phase and in Table A2 for the Rayleigh phase and in Figure A1.

### Appendix B: Additional Figures

Figure B1 shows the mean spectra for all single stations and for the unnormalized beams using 200 s long seismograms of *P* waves (dark colors) and pre-event noise (light colors). Figure B2 shows slowness bin stacks

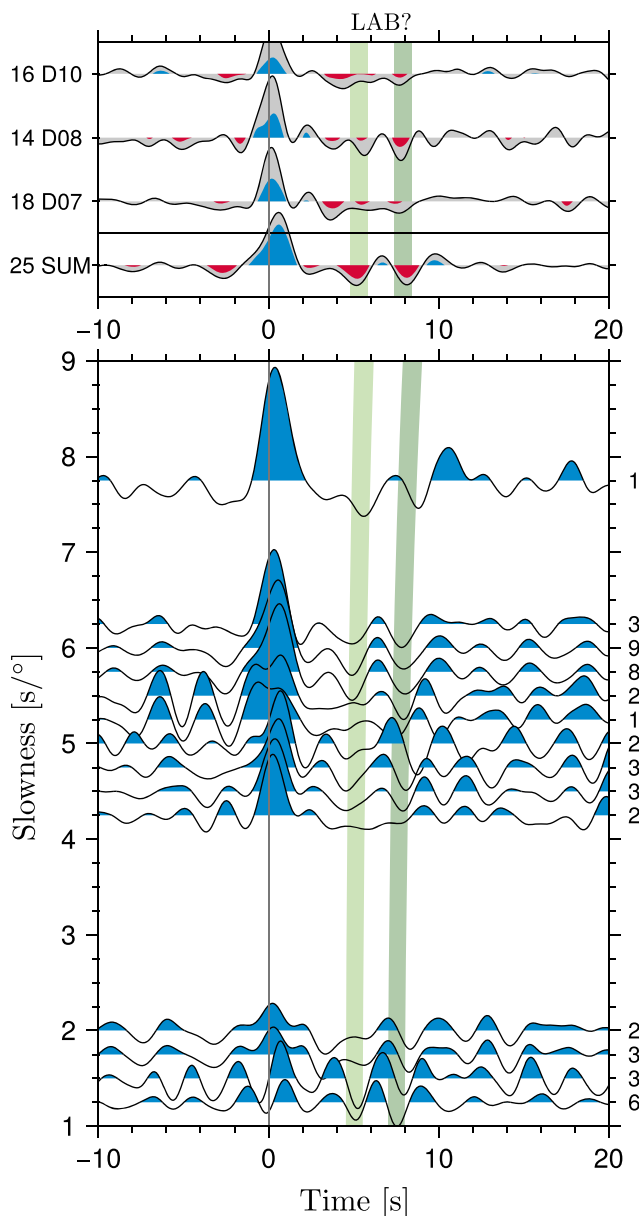


**Figure B2.** (bottom) Stacks of single stations RFs in slowness bins of  $0.5 \text{ s/}^\circ$  every  $0.25 \text{ s/}^\circ$ . Light green area shows expected delay times for an interface at 40–50 km depths and dark green area for an interface at 65–75 km assuming PREM [Dziewonski and Anderson, 1981]. The small number at the end of each slowness bin stack indicates the number of events in the bin. (top) Move-out corrected stacks for stack of all stations (SUM) and single stations D07, D08, and D10 as already presented in Figure 6a. The RFs have been band-pass filtered (2–40 s) and normalized to the *P* spike on the Z component.

for all single stations in  $0.5 \text{ s}^\circ$  wide bins every  $0.25 \text{ s}^\circ$  in comparison to theoretical move-out times for interfaces at 40–50 km and 65–75 km (green shaded areas).

### Appendix C: Event Tables

Table C1 lists the details of all events used in this study and shown in Figure 1a. Table C2 shows which event in Table C1 has been used at which station and for the beam-formed traces and gives the number of total events.

**Table C1.** Events Used for the  $P$  Receiver Functions, Origin Time, Hypocenter Location and Moment Magnitude  $M_w$  From the NEIC Catalog (earthquake.usgs.gov) Where  $\Delta$  is the Distance Between Earthquake and Array Location in Degree

#	Date (dd/mm/yyyy)	Time (hh:mm:ss.ss)	Lat (deg)	Lon (deg)	Depth (km)	$M_w$	$\Delta$ (deg)
1	06/07/2011	19:03:18.26	-29.54	-176.34	17.0	7.6	159.8
2	10/07/2011	00:57:10.80	38.03	143.26	23.0	7.0	102.1
3	29/07/2011	07:42:23.40	-23.80	179.75	532.0	6.7	158.8
4	20/08/2011	16:55:02.81	-18.37	168.14	32.0	7.2	159.3
5	24/08/2011	17:46:11.65	-7.64	-74.53	147.0	7.0	69.4
6	30/08/2011	06:57:41.61	-6.36	126.75	469.8	6.9	135.2
7	02/09/2011	10:55:53.59	52.17	-171.71	32.0	6.9	86.9
8	02/09/2011	13:47:09.62	-28.40	-63.03	578.9	6.7	78.5
9	03/09/2011	22:55:40.92	-20.67	169.72	185.1	7.0	161.0
10	05/09/2011	09:52:01.13	-15.30	-173.62	37.0	6.2	148.3
11	15/09/2011	19:31:04.08	-21.61	-179.53	644.6	7.3	156.7
12	18/09/2011	12:40:51.83	27.73	88.16	50.0	6.9	85.0
13	06/10/2011	11:12:30.07	-24.18	-64.22	15.0	5.8	75.6
14	14/10/2011	03:35:14.81	-6.57	147.88	37.0	6.5	146.0
15	21/10/2011	17:57:16.10	-28.99	-176.24	33.0	7.4	159.4
16	23/10/2011	10:41:23.25	38.72	43.51	18.0	7.1	47.6
17	28/10/2011	18:54:34.04	-14.44	-75.97	24.0	6.9	75.2
18	22/11/2011	18:48:16.30	-15.36	-65.09	549.9	6.6	69.1
19	07/12/2011	22:23:09.73	-27.90	-70.92	20.0	6.1	82.2
20	11/12/2011	01:47:25.56	17.99	-99.79	59.0	6.5	72.5
21	14/12/2011	05:04:58.63	-7.55	146.81	135.0	7.1	146.5
22	27/12/2011	15:21:56.84	51.84	95.91	15.0	6.6	73.5
23	09/01/2012	04:07:14.67	-10.62	165.16	28.0	6.4	152.2
24	10/01/2012	18:36:59.08	2.43	93.21	19.0	7.2	105.2
25	30/01/2012	05:11:00.95	-14.17	-75.64	43.0	6.4	74.8
26	02/02/2012	13:34:40.65	-17.83	167.13	23.0	7.1	159.0
27	13/02/2012	10:55:09.44	9.18	-84.12	16.0	5.9	65.4
28	26/02/2012	06:17:19.76	51.71	95.99	12.0	6.7	73.6
29	14/03/2012	09:08:35.14	40.89	144.94	12.0	6.9	99.7
30	20/03/2012	18:02:47.44	16.49	-98.23	20.0	7.4	72.1
31	21/03/2012	22:15:06.13	-6.24	145.96	118.0	6.6	145.0
32	25/03/2012	22:37:06.00	-35.20	-72.22	40.7	7.1	88.6
33	11/04/2012	08:38:36.72	2.33	93.06	20.0	8.6	105.2
34	11/04/2012	22:55:10.25	18.23	-102.69	20.0	6.5	74.6
35	12/04/2012	07:15:48.50	28.70	-113.10	13.0	7.0	76.2
36	17/04/2012	03:50:15.61	-32.63	-71.37	29.0	6.7	86.1
37	17/04/2012	07:13:49.00	-5.46	147.12	198.0	6.8	144.7

**Table C2.** Events Used at Single Stations and for P Beams<sup>a</sup>

#	D01	D02	D03	D04	D06	D07	D08	D09	D10	D11	D12	P-B
1	X	X		X	X	X	X	X	X	X	X	X
2												X
3												X
4	X											X
5	X	X	X	X	X	X	X	X	X	X	X	X
6												X
7		X	X	X	X		X	X		X		X
8		X	X	X	X	X	X	X	X	X	X	X
9			X		X	X		X	X			X
10												X
11						X	X	X				X
12									X			X
13												X
14												X
15	X	X	X	X		X	X	X	X	X	X	X
16	X	X	X	X	X	X	X	X	X	X	X	X
17	X	X		X	X	X	X	X	X	X		X
18				X	X	X		X	X		X	X
19												X
20		X		X		X						X
21		X									X	X
22									X			X
23												X
24												X
25		X			X	X				X		X
26		X			X				X	X		X
27												X
28	X	X	X	X	X	X	X	X	X	X		X
29				X	X	X						X
30	X	X	X	X	X	X	X	X	X	X	X	X
31						X	X					X
32		X	X	X	X	X			X	X	X	X
33		X		X	X	X	X		X	X	X	X
34		X	X		X		X	X		X		X
35												X
36												X
37	X	X	X	X	X	X	X	X	X	X	X	X
total	9	17	11	15	17	18	14	14	16	15	11	37

<sup>a</sup>Details of events are listed in Table C1.

**Acknowledgments**

The authors thank the DEPAS pool for providing the instruments for the DOCTAR project which was funded by the DFG (Deutsche Forschungsgemeinschaft/German Research Foundation KR1935/13 and DA478/21-1) and by the Leitstelle für Mittelgroße Forschungsschiffe (RV Poseidon cruises 416 and 431). The authors thank EMEPC (Task Group for the Extension of the Continental Shelf) for providing the bathymetric data and Luis Batista for sharing them. The data processing was partly done using Seismic Handler [Stammler, 1993]. Some figures were created using GMT [Wessel et al., 2013]. The authors thank two anonymous reviewers for their constructive comments on the manuscript. We thank Jess Hillman who helped to improve the language of the paper. The sea floor seismological data were archived by Alfred Wegener Institute (AWI), Helmholtz Centre for Polar Research, Bremerhaven, Germany, and are available upon request. The clock drifts of the OBSs are published in Hannemann et al. [2014] and the orientations in Appendix A of this study (Table A1).

**References**

Agee, C. B. (1998), Phase transformations and seismic structure in the upper mantle and transition zone, in *Ultrahigh-Pressure Mineralogy. Physics and Chemistry of the Earth's Deep Interior*, vol. 37, edited by R. J. Hemley and P. H. Ribbe, chap. 5, pp. 165–203, Mineralogical Society of America, Washington, D. C.

Aki, K., and P. G. Richards (2002), *Quantitative Seismology*, 2nd ed., 700 pp., Univ. Science Books, Sausalito, Calif.

Altenbernd, T., W. Jokat, I. Heyde, and V. Damm (2014), A crustal model for northern Melville Bay, Baffin Bay, *J. Geophys. Res. Solid Earth*, 119, 8610–8632, doi:10.1002/2014JB011559.

Audet, P. (2016), Receiver functions using OBS data: Promises and limitations from numerical modelling and examples from the Cascadia Initiative, *Geophys. J. Int.*, 205(3), 1740–1755, doi:10.1093/gji/ggw111.

- Barruol, G., and K. Sigloch (2013), Investigating La Réunion hot spot from crust to core, *Eos Trans. AGU*, 94(23), 205–207, doi:10.1002/2013EO230002.
- Bell, S. W., Y. Ruan, and D. W. Forsyth (2015), Shear velocity structure of abyssal plain sediments in Cascadia, *Seismol. Res. Lett.*, 86(5), 1247–1252, doi:10.1785/0220150101.
- Berkhout, A. J. (1977), Least-squares inverse filtering and wavelet deconvolution, *Geophysics*, 42(7), 1369–1383, doi:10.1190/1.1440798.
- Bird, P. (2003), An updated digital model of plate boundaries, *Geochem. Geophys. Geosyst.*, 4(3), 1027, doi:10.1029/2001GC000252.
- Cassidy, J. J. F. (1992), Numerical experiments in broadband receiver function analysis, *Bull. Seismol. Soc. Am.*, 82(3), 1453–1474.
- Chevrot, S., L. Vinnik, and J. P. Montagner (1999), Global-scale analysis of the mantle Pds phases, *J. Geophys. Res.*, 104(B9), 20,203–20,219, doi:10.1029/1999JB900087.
- Crawford, W. C., S. C. Webb, and J. A. Hildebrand (1998), Estimating shear velocities in the oceanic crust from compliance measurements by two-dimensional finite difference modeling, *J. Geophys. Res.*, 103(B5), 9895–9916, doi:10.1029/97JB03532.
- Czuba, W., M. Grad, R. Mjelde, A. Guterch, A. Libak, F. Krüger, Y. Murai, and J. Schweitzer (2011), Continent-ocean-transition across a trans-tensional margin segment: Off Bear Island, Barents Sea, *Geophys. J. Int.*, 184(2), 541–554, doi:10.1111/j.1365-246X.2010.04873.x.
- Dahm, T., F. Tilmann, and J. Morgan (2006), Seismic broadband ocean-bottom data and noise observed with free-fall stations: Experiences from long-term deployments in the North Atlantic and the Tyrrhenian Sea, *Bull. Seismol. Soc. Am.*, 96(2), 647–664, doi:10.1785/0120040064.
- Davy, C., G. Barruol, F. R. Fontaine, K. Sigloch, and E. Stutzmann (2014), Tracking major storms from microseismic and hydroacoustic observations on the seafloor, *Geophys. Res. Lett.*, 41, 8825–8831, doi:10.1002/2014GL062319.
- Deuss, A. (2009), Global observations of mantle discontinuities using SS and PP precursors, *Surv. Geophys.*, 30(4–5), 301–326, doi:10.1007/s10712-009-9078-y.
- Deuss, A., and J. H. Woodhouse (2002), A systematic search for mantle discontinuities using SS-precursors, *Geophys. Res. Lett.*, 29(8), 90–94, doi:10.1029/2002GL014768.
- Deuss, A., and J. H. Woodhouse (2004), The nature of the Lehmann discontinuity from its seismological Clapeyron slopes, *Earth Planet. Sci. Lett.*, 225(3–4), 295–304, doi:10.1016/j.epsl.2004.06.021.
- Deuss, A., J. Andrews, and E. Day (2013), Seismic observations of mantle discontinuities and their mineralogical and dynamical interpretation, in *Physics and Chemistry of the Deep Earth*, edited by S.-I. Karato, pp. 297–323, John Wiley, Chichester, U. K.
- Dziewonski, A. M., and D. L. Anderson (1981), Preliminary reference Earth model, *Phys. Earth Planet. Inter.*, 25(4), 297–356, doi:10.1016/0031-9201(81)90046-7.
- Efron, B., and R. Tibshirani (1986), Bootstrap methods for standard error, confidence intervals, and other measures of statistical accuracy, *Stat. Sci.*, 1(1), 54–75, doi:10.1214/ss/1177013817.
- Farra, V. V., and L. Vinnik (2000), Upper mantle stratification by P and S receiver functions, *Geophys. J. Int.*, 141(3), 699–712, doi:10.1046/j.1365-246X.2000.00118.x.
- Fischer, K. M., H. A. Ford, D. L. Abt, and C. A. Rychert (2010), The lithosphere-asthenosphere boundary, *Annu. Rev. Earth Planet. Sci.*, 38(1), 551–575, doi:10.1146/annurev-earth-040809-152438.
- Flanagan, M. P., and P. M. Shearer (1998), Global mapping of topography on transition zone velocity discontinuities by stacking SS precursors, *J. Geophys. Res.*, 103(B82), 2673–2692, doi:10.1029/97JB03212.
- Friederich, W., and T. Meier (2008), Temporary seismic broadband network acquired data on Hellenic Subduction Zone, *Eos Trans. AGU*, 89(40), 377–381, doi:10.1029/2008EO400002.
- Gao, H., and S. Schwartz (2015), Preface to the focus section on Cascadia initiative preliminary results, *Seismol. Res. Lett.*, 86(5), 1235–1237, doi:10.1785/0220150160.
- Geissler, W. H., W. Jokat, M. Jegen, and K. Baba (2016), Thickness of the oceanic crust, the lithosphere, and the mantle transition zone in the vicinity of the Tristan da Cunha hot spot estimated from ocean-bottom and ocean-island seismometer receiver functions, *Tectonophysics*, doi:10.1016/j.tecto.2016.12.013.
- Gilbert, H. J., A. F. Sheehan, D. A. Wiens, K. G. Dueker, L. M. Dorman, J. Hildebrand, and S. Webb (2001), Upper mantle discontinuity structure in the region of the Tonga Subduction Zone, *Geophys. Res. Lett.*, 28(9), 1855–1858, doi:10.1029/2000GL012192.
- Gossler, J., and R. Kind (1996), Seismic evidence for very deep roots of continents, *Earth Planet. Sci. Lett.*, 138(1–4), 1–13, doi:10.1016/0012-821X(95)00215-X.
- Grad, M., R. Mjelde, W. Czuba, A. Guterch, and IPY Project Group (2012), Elastic properties of seafloor sediments from the modelling of amplitudes of multiple water waves recorded on the seafloor off Bear Island, North Atlantic, *Geophys. Prospect.*, 60(5), 855–869, doi:10.1111/j.1365-2478.2011.01022.x.
- Grevenmeyer, I., T. J. Reston, and S. Moeller (2013), Microseismicity of the Mid-Atlantic Ridge at 7°S–8°15'S and at the Logatchev Massif oceanic core complex at 14°40'N–14°50'N, *Geochem. Geophys. Geosyst.*, 14(9), 3532–3554, doi:10.1002/ggge.20197.
- Grevenmeyer, I., E. Gràcia, A. Villaseñor, W. Leuchters, and A. B. Watts (2015), Seismicity and active tectonics in the Alboran Sea, Western Mediterranean: Constraints from an offshore-onshore seismological network and swath bathymetry data, *J. Geophys. Res. Solid Earth*, 120, 8348–8365, doi:10.1002/2015JB012073.
- Grigoli, F., S. Cesca, T. Dahm, and L. Krieger (2012), A complex linear least-squares method to derive relative and absolute orientations of seismic sensors, *Geophys. J. Int.*, 188(3), 1243–1254, doi:10.1111/j.1365-246X.2011.05316.x.
- Gu, Y. J., and A. M. Dziewonski (2002), Global variability of transition zone thickness, *J. Geophys. Res.*, 107(B7), 2135, doi:10.1029/2001JB000489.
- Gu, Y. J., A. M. Dziewonski, and C. B. Agee (1998), Global de-correlation of transition zone discontinuities, *Earth Planet. Sci. Lett.*, 157(1–2), 57–67.
- Hannemann, K., F. Krüger, and T. Dahm (2014), Measuring of clock drift rates and static time offsets of ocean bottom stations by means of ambient noise, *Geophys. J. Int.*, 196(2), 1034–1042, doi:10.1093/gji/ggt434.
- Hannemann, K., F. Krüger, T. Dahm, and D. Lange (2016), Oceanic lithospheric S-wave velocities from the analysis of P-wave polarization at the ocean floor, *Geophys. J. Int.*, 207(3), 1796–1817, doi:10.1093/gji/ggw342.
- Helfrich, G. (2000), Topography of the transition zone seismic discontinuities, *Rev. Geophys.*, 38(1), 141–158, doi:10.1029/1999RG000060.
- Hermann, T., and W. Jokat (2013), Crustal structures of the boreas basin and the Knipovich Ridge, North Atlantic, *Geophys. J. Int.*, 193(3), 1399–1414, doi:10.1093/gji/ggt048.
- Janiszewski, H. A., and G. A. Abers (2015), Imaging the plate interface in the Cascadia Seismogenic Zone: New constraints from offshore receiver functions, *Seismol. Res. Lett.*, 86(5), 1261–1269, doi:10.1785/0220150104.
- Jokat, W., J. Kollofrath, W. H. Geissler, and L. Jensen (2012), Crustal thickness and earthquake distribution south of the Logachev Seamount, Knipovich Ridge, *Geophys. Res. Lett.*, 39(8), 2–7, doi:10.1029/2012GL051199.

- Julià, J. (2007), Constraining velocity and density contrasts across the crust-mantle boundary with receiver function amplitudes, *Geophys. J. Int.*, *171*(1), 286–301, doi:10.1111/j.1365-2966.2007.3502.x.
- Kalberg, T., and K. Gohl (2014), The crustal structure and tectonic development of the continental margin of the Amundsen Sea embayment, West Antarctica: Implications from geophysical data, *Geophys. J. Int.*, *198*(1), 327–341, doi:10.1093/gji/ggu118.
- Karato, S.-i. (1992), On the Lehmann discontinuity, *Geophys. Res. Lett.*, *19*(22), 2255–2258, doi:10.1029/92GL02603.
- Karato, S.-i. (2012), On the origin of the asthenosphere, *Earth Planet. Sci. Lett.*, *321*–322, 95–103, doi:10.1016/j.epsl.2012.01.001.
- Karato, S.-i., and H. Jung (1998), Water, partial melting and the origin of the seismic low velocity and high attenuation zone in the upper mantle, *Earth Planet. Sci. Lett.*, *157*(3–4), 193–207, doi:10.1016/S0012-821X(98)00034-X.
- Kawakatsu, H., and Y. Abe (2016), Comment on “Nature of the Seismic Lithosphere-Asthenosphere Boundary within Normal Oceanic Mantle from High-Resolution Receiver Functions” by Ulugboji et al., *Geochem. Geophys. Geosyst.*, *17*(8), 3488–3492, doi:10.1002/2016GC006418.
- Kawakatsu, H., P. Kumar, Y. Takei, M. Shinohara, T. Kanazawa, E. Araki, and K. Suyehiro (2009), Seismic evidence for sharp lithosphere-asthenosphere boundaries of oceanic plates, *Science*, *324*(5926), 499–502, doi:10.1126/science.1169499.
- Kind, R., G. L. Kosarev, and N. V. Petersen (1995), Receiver functions at the stations of the German Regional Seismic Network (GRSN), *Geophys. J. Int.*, *121*(1), 191–202, doi:10.1111/j.1365-246X.1995.tb03520.x.
- Kopp, H., et al. (2011), Deep structure of the central Lesser Antilles Island Arc: Relevance for the formation of continental crust, *Earth Planet. Sci. Lett.*, *304*(1–2), 121–134, doi:10.1016/j.epsl.2011.01.024.
- Kumar, P., and H. Kawakatsu (2011), Imaging the seismic lithosphere-asthenosphere boundary of the oceanic plate, *Geochem. Geophys. Geosyst.*, *12*(1), Q01006, doi:10.1029/2010GC003358.
- Laigle, M., et al. (2013), Seismic structure and activity of the north-central Lesser Antilles subduction zone from an integrated approach: Similarities with the Tohoku forearc, *Tectonophysics*, *603*, 1–20, doi:10.1016/j.tecto.2013.05.043.
- Langston, C. A. (1979), Structure under Mount Rainier, Washington, inferred from teleseismic body waves, *J. Geophys. Res.*, *84*(B9), 4749–4762, doi:10.1029/JB084iB09p04749.
- Laske, G., G. Masters, Z. Ma, and M. E. Pasyanos (2013), *CRUST1.0: An Updated Global Model of Earth's Crust*, Geophys. Res. Abstr., vol. 15, EGU2013-2658, Vienna.
- Lawrence, J. F., and P. M. Shearer (2006), A global study of transition zone thickness using receiver functions, *J. Geophys. Res.*, *111*, B06307, doi:10.1029/2005JB003973.
- Lehmann, I. (1961), S and the structure of the upper mantle, *Geophys. J. Int.*, *4*, 124–138, doi:10.1111/j.1365-246X.1937.tb07108.x.
- Li, X., S. V. Sobolev, R. Kind, X. Yuan, and C. Estabrook (2000), A detailed receiver function image of the upper mantle discontinuities in the Japan subduction zone, *Earth Planet. Sci. Lett.*, *183*(3–4), 527–541, doi:10.1016/S0012-821X(00)00294-6.
- Libak, A., R. Mjelde, H. Keers, J. I. Faleide, and Y. Murai (2012), An integrated geophysical study of Vestbakken Volcanic Province, western Barents Sea continental margin, and adjacent oceanic crust, *Mar. Geophys. Res.*, *33*(2), 185–207, doi:10.1007/s11001-012-9155-3.
- Lin, P.-y. P., J. B. Gaherty, G. Jin, J. A. Collins, D. Lizarralde, R. L. Evans, and G. Hirth (2016), High-resolution seismic constraints on flow dynamics in the oceanic asthenosphere, *Nature*, *535*(7613), 538–541, doi:10.1038/nature18012.
- McNamara, D. E. (2004), Ambient noise levels in the Continental United States, *Bull. Seismol. Soc. Am.*, *94*(4), 1517–1527, doi:10.1785/012003001.
- Monna, S., G. B. Cimini, C. Montuori, L. Matias, W. H. Geissler, and P. Favali (2013), New insights from seismic tomography on the complex geodynamic evolution of two adjacent domains: Gulf of Cadiz and Alboran Sea, *J. Geophys. Res. Solid Earth*, *118*, 1587–1601, doi:10.1029/2012JB009607.
- Müller, R. D., M. Sdrolias, C. Gaina, and W. R. Roest (2008), Age, spreading rates, and spreading asymmetry of the world's ocean crust, *Geochem. Geophys. Geosyst.*, *9*(4), Q04006, doi:10.1029/2007GC001743.
- Olugboji, T. M., S. Karato, and J. Park (2013), Structures of the oceanic lithosphere-asthenosphere boundary: Mineral-physics modeling and seismological signatures, *Geochem. Geophys. Geosyst.*, *14*(4), 880–901, doi:10.1002/ggge.20086.
- Olugboji, T. M., J. Park, S.-i. Karato, and M. Shinohara (2016), Nature of the seismic lithosphere-asthenosphere boundary within normal oceanic mantle from high-resolution receiver functions, *Geochem. Geophys. Geosyst.*, *17*(4), 1265–1282, doi:10.1002/2015GC006214.
- Piilidou, S., K. Priestley, E. Debayle, and Ó. Gudmundsson (2005), Rayleigh wave tomography in the North Atlantic: High resolution images of the Iceland, Azores and Eifel mantle plumes, *Lithos*, *79*(3–4), 453–474, doi:10.1016/j.lithos.2004.09.012.
- Robinson, E., and S. Treitel (1980), *Geophysical Signal Analysis*, Prentice Hall, Englewood Cliffs, N. J.
- Romanowicz, B. (2009), The thickness of tectonic plates, *Science*, *324*(5926), 474–476, doi:10.1126/science.1172879.
- Rost, S., and C. Thomas (2002), Array seismology: Methods and applications, *Rev. Geophys.*, *40*(3), 1008, doi:10.1029/2000RG000100.
- Ruiz, M., et al. (2013), Seismic activity offshore Martinique and Dominica islands (Central Lesser Antilles subduction zone) from temporary onshore and offshore seismic networks, *Tectonophysics*, *603*, 68–78, doi:10.1016/j.tecto.2011.08.006.
- Ryberg, T., W. Geissler, W. Jokat, and S. Pandey (2017), Uppermost mantle and crustal structure at Tristan da Cunha derived from ambient seismic noise, *Earth Planet. Sci. Lett.*, *471*, 117–124, doi:10.1016/j.epsl.2017.04.049.
- Rychert, C. A., N. Schmerr, and N. Harmon (2012), The Pacific lithosphere-asthenosphere boundary: Seismic imaging and anisotropic constraints from SS waveforms, *Geochem. Geophys. Geosyst.*, *13*(9), 1–18, doi:10.1029/2012GC004194.
- Saki, M., C. Thomas, S. E. J. Nippres, and S. Lessing (2015), Topography of upper mantle seismic discontinuities beneath the North Atlantic: The Azores, Canary and Cape Verde plumes, *Earth Planet. Sci. Lett.*, *409*, 193–202, doi:10.1016/j.epsl.2014.10.052.
- Savage, M. K. (1998), Lower crustal anisotropy or dipping boundaries? Effects on receiver functions and a case study in New Zealand, *J. Geophys. Res.*, *103*(B7), 15,069–15,087, doi:10.1029/98JB00795.
- Scherbaum, F. (2001), *Of Poles and Zeros, Modern Approaches in Geophysics*, 2nd ed., vol. 15, 335 pp., Springer, Dordrecht, Netherlands.
- Schlindwein, V., A. Demuth, W. H. Geissler, and W. Jokat (2013), Seismic gap beneath Logachev Seamount: Indicator for melt focusing at an ultraslow mid-ocean ridge?, *Geophys. Res. Lett.*, *40*, 1703–1707, doi:10.1002/grl.50329.
- Schlindwein, V., A. Demuth, E. Kogger, C. Läderach, and F. Schmid (2015), Seismicity of the Arctic mid-ocean ridge system, *Polar Sci.*, *9*(1), 146–157, doi:10.1016/j.polar.2014.10.001.
- Sheehan, A. F., G. A. Abers, C. H. Jones, and A. L. Lerner-Lam (1995), Crustal thickness variations across the Colorado Rocky Mountains from teleseismic receiver functions, *J. Geophys. Res.*, *100*(B10), 20,391–20,404, doi:10.1029/95JB01966.
- Shen, Y., A. F. Sheehan, K. G. Dueker, C. de Groot-Hedlin, and H. Gilbert (1998a), Mantle discontinuity structure beneath the southern east Pacific Rise from P-to-S converted phases, *Science*, *280*(5367), 1232–1235, doi:10.1126/science.280.5367.1232.
- Shen, Y., S. C. Solomon, I. T. Bjarnason, and C. J. Wolfe (1998b), Seismic evidence for a lower-mantle origin of the Iceland plume, *Nature*, *395*(6697), 62–65, doi:10.1038/25714.
- Silveira, G., L. Vinnik, E. Stutzmann, V. Farra, S. Kiselev, and I. Morais (2010), Stratification of the Earth beneath the Azores from P and S receiver functions, *Earth Planet. Sci. Lett.*, *299*(1–2), 91–103, doi:10.1016/j.epsl.2010.08.021.



- Stachnik, J. C., A. F. Sheehan, D. W. Zietlow, Z. Yang, J. Collins, and A. Ferris (2012), Determination of New Zealand Ocean bottom seismometer orientation via Rayleigh-Wave polarization, *Seismol. Res. Lett.*, *83*(4), 704–713, doi:10.1785/0220110128.
- Stähler, S. C., K. Sigloch, K. Hosseini, W. C. Crawford, G. Barruol, M. C. Schmidt-Aursch, M. Tsekhmistrenko, J. R. Scholz, A. Mazzullo, and M. Deen (2016), Performance report of the RHUM-RUM ocean bottom seismometer network around La Réunion, western Indian Ocean, *Adv. Geosci.*, *41*, 43–63, doi:10.5194/adgeo-41-43-2016.
- Stammler, K. (1993), Seismichandler—Programmable multichannel data handler for interactive and automatic processing of seismological analyses, *Comput. Geosci.*, *19*(2), 135–140, doi:10.1016/0098-3004(93)90110-Q.
- Suckro, S. K., K. Gohl, T. Funck, I. Heyde, A. Ehrhardt, B. Schreckenberger, J. Gerlings, V. Damm, and W. Jokat (2012), The crustal structure of southern Baffin Bay: Implications from a seismic refraction experiment, *Geophys. J. Int.*, *190*(1), 37–58, doi:10.1111/j.1365-246X.2012.05477.x.
- Suetsugu, D., and H. Shiobara (2014), Broadband ocean-bottom seismology, *Annu. Rev. Earth Planet. Sci.*, *42*(1), 27–43, doi:10.1146/annurev-earth-060313-054818.
- Suetsugu, D., et al. (2005), Mantle discontinuity depths beneath the west Philippine basin from receiver function analysis of deep-sea borehole and seafloor broadband waveforms, *Bull. Seismol. Soc. Am.*, *95*(5), 1947–1956, doi:10.1785/0120040169.
- Suetsugu, D., H. Shiobara, H. Sugioka, Y. Fukao, and T. Kanazawa (2007), Topography of the mantle discontinuities beneath the South Pacific superswell as inferred from broadband waveforms on seafloor, *Phys. Earth Planet. Inter.*, *160*(3–5), 310–318, doi:10.1016/j.pepi.2006.11.011.
- Suetsugu, D., et al. (2010), Depths of the 410-km and 660-km discontinuities in and around the stagnant slab beneath the Philippine Sea: Is water stored in the stagnant slab?, *Phys. Earth Planet. Inter.*, *183*(1–2), 270–279, doi:10.1016/j.pepi.2010.09.004.
- Sumy, D. F., J. A. Lodewyk, R. L. Woodward, and B. Evers (2015), Ocean-bottom seismograph performance during the Cascadia initiative, *Seismol. Res. Lett.*, *86*(5), 1238–1246, doi:10.1785/0220150110.
- Takei, Y., F. Karasawa, and H. Yamauchi (2014), Temperature, grain size, and chemical controls on polycrystal anelasticity over a broad frequency range extending into the seismic range, *J. Geophys. Res. Solid Earth*, *119*(7), 5414–5443, doi:10.1002/2014JB011146.
- Takeo, A., K. Nishida, T. Isse, H. Kawakatsu, H. Shiobara, H. Sugioka, and T. Kanazawa (2013), Radially anisotropic structure beneath the Shikoku Basin from broadband surface wave analysis of ocean bottom seismometer records, *J. Geophys. Res. Solid Earth*, *118*, 1–15, doi:10.1002/jgrb.50219.
- Takeo, A., H. Kawakatsu, T. Isse, K. Nishida, H. Sugioka, A. Ito, H. Shiobara, and D. Suetsugu (2016), Seismic azimuthal anisotropy in the oceanic lithosphere and asthenosphere from broadband surface wave analysis of OBS array records at 60 Ma seafloor, *J. Geophys. Res. Solid Earth*, *121*(3), 1927–1947, doi:10.1002/2015JB012429.
- Tauzin, B., E. Debayle, and G. Wittlinger (2008), The mantle transition zone as seen by global  $Pd_s$  phases: No clear evidence for a thin transition zone beneath hotspots, *J. Geophys. Res.*, *113*, B08309, doi:10.1029/2007JB005364.
- Thomas, C., and G. Laske (2015),  $D''$  observations in the Pacific from PLUME ocean bottom seismometer recordings, *Geophys. J. Int.*, *200*(2), 849–860, doi:10.1093/gji/ggu441.
- Thorwart, M. (2006), Confirming wavefield methods to analyze passive ocean bottom seismic data. Application to the Tyrrhenian Sea, PhD thesis, Universität Hamburg, Germany.
- Thorwart, M., and T. Dahm (2005), Wavefield decomposition for passive ocean bottom seismological data, *Geophys. J. Int.*, *163*(2), 611–621, doi:10.1111/j.1365-246X.2005.02761.x.
- Tilmann, F. J., and T. Dahm (2008), Constraints on crustal and mantle structure of the oceanic plate south of Iceland from ocean bottom recorded Rayleigh waves, *Tectonophysics*, *447*(1–4), 66–79, doi:10.1016/j.tecto.2006.02.028.
- Vinnik, L. P. (1977), Detection of waves converted from P to SV in the mantle, *Phys. Earth Planet. Inter.*, *15*(1), 39–45, doi:10.1016/0031-9201(77)90008-5.
- Wang, R. (1999), A simple orthonormalization method for stable and efficient computation of Green's functions, *Bull. Seismol. Soc. Am.*, *89*(3), 733–741.
- Webb, S. C. (1998), Broadband seismology and noise under the ocean, *Rev. Geophys.*, *36*(1), 105–142, doi:10.1029/97RG02287.
- Wessel, P., W. H. F. Smith, R. Scharroo, J. Luis, and F. Wobbe (2013), Generic mapping tools: Improved version released, *Eos Trans. AGU*, *94*(45), 409–410, doi:10.1002/2013EO450001.
- White, R. S., D. McKenzie, and R. K. O'Nions (1992), Oceanic crustal thickness from seismic measurements and rare earth element inversions, *J. Geophys. Res.*, *97*(B13), 19,683–19,715, doi:10.1029/92JB01749.
- Yamauchi, H., and Y. Takei (2016), Polycrystal anelasticity at near-solidus temperatures, *J. Geophys. Res. Solid Earth*, *121*(11), 7790–7820, doi:10.1002/2016JB013316.
- Yilmaz, Ö. (2008), *Seismic Data Analysis: Processing, Inversion, and Interpretation of Seismic Data*, 2nd ed., 2065 pp., Society of Exploration Geophysicists (SEG), Tulsa, Okla.
- Yuan, X., J. Ni, R. Kind, J. Mechie, and E. Sandvol (1997), Lithospheric and upper mantle structure of southern Tibet from a seismological passive source experiment, *J. Geophys. Res.*, *102*(B12), 27,491–27,500, doi:10.1029/97JB02379.
- Zha, Y., S. C. Webb, and W. Menke (2013), Determining the orientations of ocean bottom seismometers using ambient noise correlation, *Geophys. Res. Lett.*, *40*, 3585–3590, doi:10.1002/grl.50698.